Tectonic evolution of the northeastern Pamir: Constraints from the northern portion of the Cenozoic Kongur Shan extensional system, western China

Alexander C. Robinson[†]
An Yin[‡]
Craig E. Manning[§]
T. Mark Harrison[#]
Department of Earth and Space Sciences and Institute of Geophysics and Planetary Physics, University of California, Los Angeles, California, 90095-1567, USA
Shuan-Hong Zhang[††]
Xiao-Feng Wang[‡‡]
Institute of Geomechanics, Chinese Academy of Geological Sciences, Beijing 100081, People's Republic of China

ABSTRACT

The late Cenozoic Kongur Shan extensional system lies along the northeastern margin of the Pamir at the western end of the Himalayan-Tibetan orogen, accommodating east-west extension in the Pamir. At the northern end of the extensional system, the Kongur Shan normal fault juxtaposes medium- to high-grade metamorphic rocks in both its hanging wall and footwall, which record several Mesozoic to Cenozoic tectonic events. Schists within the hanging wall preserve a Buchan metamorphic sequence, dated as Late Triassic to Early Jurassic (230–200 Ma) from monazite inclusions in garnet. Metamorphic ages overlap with U-Pb zircon ages from local granite bodies and are interpreted to be the result of regional arc magmatism created by subduction of the Paleo-Tethys ocean. The northern portion of the footwall of the extensional system exposes an upper-amphibolite-facies unit (~650 °C, 8 kbar), which structurally overlies a low-grade metagraywacke unit. The high-grade unit records late Early Cretaceous crustal thickening at ca. 125–110 Ma, followed by emplacement over the low-grade metagraywacke along a north-northeast–directed thrust prior to ca. 100 Ma. Together these results indicate significant middle Cretaceous crustal thickening and shortening in the northern Pamir prior to the Indo-Asian collision. A third Late Miocene (ca. 9 Ma) amphibolite-facies metamorphic event (~650–700 °C, 8 kbar) is recorded in footwall gneisses of the Kongur Shan massif. North of the Kongur Shan massif, rapid cooling in the footwall beginning at 7–8 Ma is interpreted to date the initiation of exhumation along the Kongur Shan normal fault. A minimum of 34 km of east-west extension is inferred along the Kongur Shan massif based on the magnitude of exhumation since the Late Miocene (~29 km) and the present dip of the Kongur Shan normal fault (~40°). Field observations and interpretation of satellite images along the southernmost segment of the Kongur Shan extensional system indicate that the magnitude of late Cenozoic east-west extension decreases significantly toward the south. This observation is inconsistent with models in which east-west extension in the Pamir is driven by northward propagation of the right-slip Karakoram fault, suggesting instead that extension is driven by vertical extrusion due to topographic collapse, radial thrusting along the Main Pamir Thrust, or oroclinal bending of the entire Pamir region.

Keywords: Pamir, tectonics, metamorphism, age determination, extension, crustal shortening.

INTRODUCTION

A prominent feature of the Indo-Asian collision zone is the pronounced asymmetry in the region of thickened and elevated crust immediately north of the Indian craton. In map view, the north-south width of thickened crust changes dramatically from ~500 km in the west across the Pamir and western Himalayan syntaxis region to >1500 km in the central and eastern portions of the Tibetan Plateau (Fig. 1A). Three end-member models have been proposed to explain the development of this asymmetry: (1) different magnitudes of convergence between India and Asia between the eastern and western Himalayan syntaxes (e.g., Dewey et al., 1988, 1989; Le Pichon et al., 1992), (2) eastward lateral extrusion of Tibetan crust (Molnar and Tapponnier, 1975; Tapponnier et al., 1982; Peltzer and Tapponnier, 1988), and (3) distributed shortening across the Indo-Asian collision zone interacting with lateral heterogeneities in the strength of the Asian crust (i.e., Tarim basin) (England and Houseman, 1985; Houseman and England, 1996; Neil and Houseman, 1997). As an alternative to these conceptual models, based on offset of the Western and Eastern Kunlun batholiths, Cowgill et al. (2003) suggest that the asymmetry of the Tibetan Plateau is a result of the development of Tertiary thrust belts with opposite polarities linked by the left-slip Altyn Tagh fault.

The observations by Cowgill et al. (2003), as well as documented Tertiary strike-slip faulting and crustal shortening in western Tibet (Ratschbacher et al., 1994; Matte et al., 1996; Searle et al., 1998; Kapp et al., 2003), suggest that both lateral extrusion and distributed shortening have occurred synchronously. However, the relative contribution of these mechanisms in the evolution of the Indo-Asian collision belt, and the asymmetry of the Himalayan-Tibetan orogen, remains poorly understood (e.g., Le Pichon et al., 1992; Johnson, 2002). Key to determining the relative contributions of these different deformation mechanisms is understanding the differences in the tectonic evolution between the western

[†]E-mail: robinson@ess.ucla.edu.
[‡]E-mail: yin@ess.ucla.edu.
[§]E-mail: manning@ess.ucla.edu.
[#]E-mail: tmh@argon.ess.ucla.edu.
[††]E-mail: zhangshuanhong@sina.com.
[‡‡]E-mail: wxf@cags.net.cn.

GSA Bulletin; July/August 2004; v. 116; no. 7/8; p. 953–973; doi: 10.1130/B25375.1; 21 figures; 2 tables; Data Repository item 2004107.

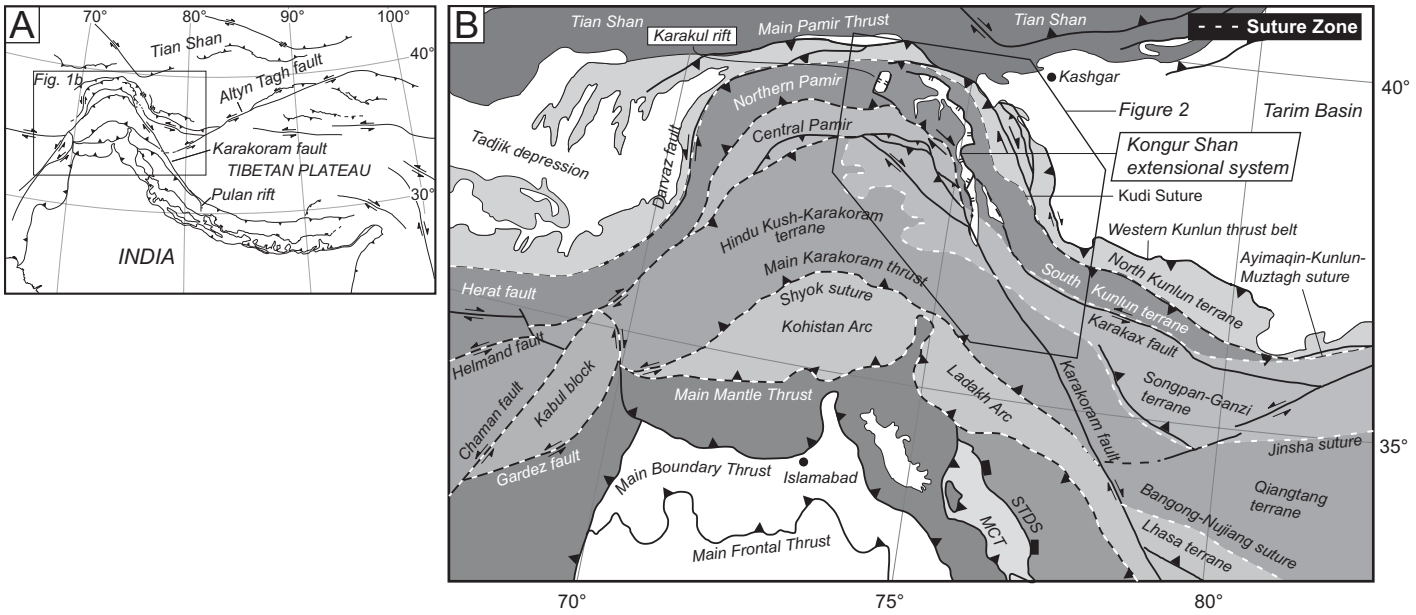

Figure 1. (A) Simplified regional tectonic map of the Himalayan-Tibetan orogen. (B) Tectonic map of the Pamir–western Himalayan syntaxis showing tectonic terranes and major Cenozoic structures, after Tapponnier et al. (1981), Burtman and Molnar (1993), Treloar and Izatt (1993), Brunel et al. (1994), Strecker et al. (1995), Schneider et al. (1999), Rumelhart et al. (1999), Yin et al. (2002), and Cowgill et al. (2003). STDS—South Tibetan Detachment, MCT—Main Central Thrust.

segment (the Pamir–western Himalayan syntaxis) and central and eastern segments (the Tibetan Plateau) of the Himalayan-Tibetan orogenic belt.

Tectonic Setting

The Pamir–western Himalayan syntaxis lies at the western end of the Indo-Asian collision zone and is bounded by the Main Pamir Thrust to the north, and the Main Boundary Thrust and Main Frontal Thrust to the south (Fig. 1B). The Main Pamir Thrust is a crustal-scale fault, interpreted to have accommodated northward translation of the Pamir ~300 km over the Tarim basin, Tadjik basin, and Alai Valley (Burtman and Molnar, 1993; Brunel et al., 1994; Strecker et al., 1995; Matte et al., 1996; Pavlis et al., 1997; Sobel and Dumitru, 1997; Arrowsmith and Strecker, 1999). To the east, the Main Pamir Thrust links with the Western Kunlun thrust belt, which forms the southwest termination for the left-slip Altyn Tagh fault (Burchfiel et al., 1989; Yin et al., 2002; Cowgill et al., 2003). The large magnitude of northward displacement of the Pamir salient has resulted in the development of right-slip faults along the eastern margin of the salient (e.g., the Kumtagh fault of Sobel and Dumitru, 1997) and left-slip faults along the western margin of the salient (e.g., the Darvaz fault, Burtman and Molnar, 1993) (Fig. 1B). Like the Main Pamir Thrust, the Main Boundary and Main Frontal Thrusts in the southern Himalayas are crustal-scale faults accommodating northward underthrusting of India beneath Asia.

Earthquake hypocenter relocations indicate active intracontinental subduction beneath the Pamir–western Himalayan syntaxis (Burtman and Molnar, 1993; Fan et al., 1994; Pegler and Das, 1998). Interpretation of relocated seismic events along the southern margin of the Pamir–western Himalayan syntaxis region suggest shallow north-directed subduction of the Indian plate beneath Asia (Fan et al., 1994; Pegler and Das, 1998). A steeply south-dipping zone of seismicity under the Pamir reaches depths of ~200 km, and projects to the surface trace of the Main Pamir thrust (Burtman and Molnar, 1993). Interpretation of this zone is controversial and has been described as either southward-subducted Asian lithosphere (Burtman and Molnar, 1993; Fan et al., 1994) or a rotated portion of subducted Indian lithosphere (Pegler and Das, 1998; Pavlis and Das, 2000).

The eastern margin of the Pamir–western Himalayan syntaxis region is bounded by the ~1000-km-long right-slip Karakoram fault, which extends from the eastern Pamir to southwestern Tibet (Fig. 1B). Determining the slip history of the Karakoram fault is essential for understanding the evolution of the region, as it provides constraints on (1) the role and magnitude of eastward extrusion (Peltzer and Tapponnier, 1988), (2) correlations between the geology of the Pamir–western syntaxis and western Tibet (Hodges, 2000), and (3) the role and history of strain transfer between thrust belts and extensional systems of the Pamir and western Tibet (Ratschbacher et al., 1994; Murphy et al., 2000). Studies along the central segment of the Karakoram fault document 120–150 km of right-slip motion initiating in the Middle Miocene (Searle, 1996; Dunlap et al., 1998; Searle et al., 1998). Additionally, studies along the southern portion of the Karakoram fault have indicated that Late Miocene southward propagation of the fault resulted in 66 ± 5.5 km of right-slip displacement, as well as the development of the north-south–striking Pulan rift and Gurla Mandhata detachment system (Murphy et al., 2000, 2002). These studies suggest that the Karakoram fault has played a minor role in the eastward extrusion of Tibetan crust (i.e., <150 km, cf. Armijo et al., 1986, 1989).

In the Pamir–western Himalayan syntaxis region, Cenozoic deformation appears to have been dominated by north-south shortening along east-trending structures (e.g., the Main Mantle Thrust, Main Karakoram Thrust, Rushan Pshart zone, and Main Pamir Thrust) (Fig. 1B) (Burtman and Molnar, 1993). However, active deformation in the region is dominated by north-trending faults and folds, accommodating east-west shortening in the Nanga Parbat massif in the south (Madin et al., 1989; Schneider et al., 1999; Zeitler et al., 2001) and east-west extension along the Kongur Shan extensional system

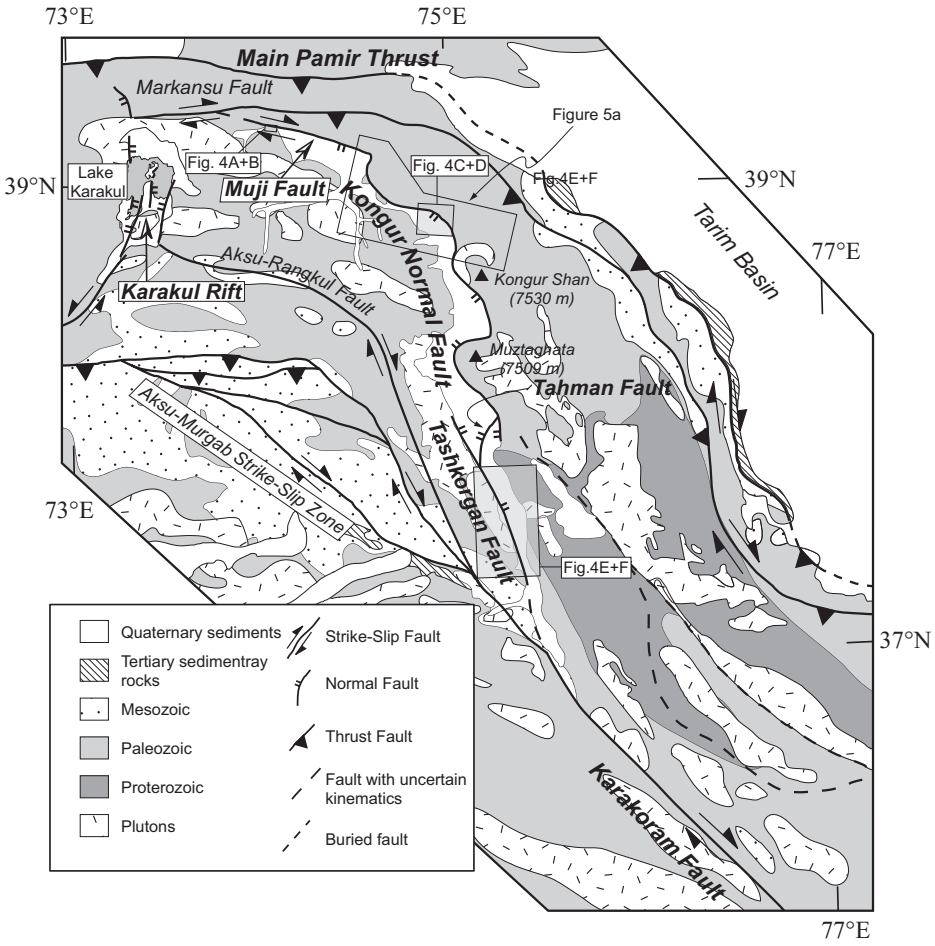

Figure 2. Simplified geologic map of the northeastern Pamir (after Yin and Bian, 1992; Brunel et al., 1994; Strecker et al., 1995) showing distribution of lithologic ages and major late Cenozoic faults. The active Kongur Shan extensional system is composed of four main fault segments based on geometric and kinematic differences: the Muji fault, the Kongur Shan fault, the Tahman fault, and the Tashkorgan fault. Areas depicted in satellite images in Figure 4 are shown as gray boxes.

and Karakul rift in the north (Brunel et al., 1994; Strecker et al., 1995; Blisniuk and Strecker, 1996) (Figs. 1B and 2). Recent studies along the Nanga Parbat–western syntaxis (Schneider et al., 1999; Zeitler et al., 2001) and gneiss domes of the Ladakh terrane (Maheo et al., 2002) suggest a tectonic evolution controlled by localized strain partitioning (i.e., local buckling of the crust, arc-parallel shortening, or a "tectonic aneurysm": Seeber and Pecher, 1998; Burg and Podladchikov, 2000; Zeitler et al., 2001). However, the evolution of east-west extension in the Pamir, and the mechanism behind it, remain relatively poorly understood.

Pre-Cenozoic Tectonics

The Pamir–western Himalayan syntaxis region is composed of terranes accreted to the southern margin of Asia during the Paleozoic through Mesozoic, and are along-strike equivalents of terranes identified to the east within the Tibetan Plateau and to the west in Afghanistan (Fig. 1B) (Tapponnier et al., 1981; Burtman and Molnar, 1993; Pan, 1996; Yin and Harrison, 2000). From north to south, these are the North Kunlun terrane, northern Pamir (South Kunlun terrane), central Pamir (the Rushan Pshart zone), Karakoram terrane, and Kohistan-Ladakh arc terrane. While correlating the Karakoram terrane across the right-slip Karakoram fault to the Qiangtang or Lhasa terranes of the Tibetan Plateau has been a matter of debate, relatively low magnitudes of slip along the Karakoram fault (120–150 km: Searle, 1996; Searle et al., 1998) (60–70 km: Murphy et al., 2000) indicate that the Karakoram terrane is equivalent to the Qiangtang terrane (Yin and Harrison, 2000). The Lhasa and Kohistan-Ladakh terranes are considered part of a continuous magmatic arc by Yin and Harrison (2000). They suggest that the arc has a continental basement equivalent to the Lhasa terrane in the Ladakh region (Dewey et al., 1988), while the arc was built on oceanic crust in the Kohistan terrane (Khan et al., 1993; Searle et al., 1999). Kapp et al. (2003) explain the abrupt decrease in the width of the Lhasa terrane across the Karakoram fault, and the lack of continental rocks between the Kohistan and Karakoram terranes, as a result of partial to complete northward underthrusting of the Lhasa terrane beneath the Qiangtang-Karakoram terrane.

The successive accretion of terranes during the Mesozoic has been interpreted to have caused deformation throughout the southern margin of Asia, reactivating tectonic belts as far north as the Tian Shan mountains during the Mesozoic (e.g., Hendrix et al., 1992; Dumitru et al., 2001). An increasing body of evidence within the Tibetan Plateau and along its margins suggests that prior to the Indo-Asian collision, the southern portion of Asia was already moderately thickened and possibly elevated (Burg and Chen, 1984; Murphy et al., 1997; Hildebrande et al., 2001; Kapp et al., 2003; Robinson et al., 2003), partially as a result of these multiple accretion events. Understanding the extent of pre-Cenozoic crustal shortening and thickening is therefore critical when calculating crustal budgets for the Indo-Asian collision (e.g., Le Pichon et al., 1992; Johnson, 2002).

Late Cenozoic Extension in the Pamir: Previous Work and Existing Models

East-west extension in the Pamir is accommodated along two primary structures: the 250-km-long Kongur Shan extensional system of the northeastern Pamir (Arnaud et al., 1993; Brunel et al., 1994) and the Karakul rift of the central northern Pamir (Strecker et al., 1995; Blisniuk and Strecker, 1996) (Fig. 2). Both fault systems show evidence of recent activity, and previous investigations have provided important first-order constraints on the timing and kinematics of extension. Arnaud et al. (1993) and Brunel et al. (1994) first documented rapid Late Miocene to Recent exhumation along the west-dipping Kongur Shan normal fault (Fig. 2) with muscovite $^{40}Ar/^{39}Ar$ ages as young as 1.9 Ma from footwall mylonites. The Karakul rift lies along the northern margin of the Pamir (Fig. 2) and is defined by steeply east- and west-dipping normal faults, bounded by active strike-slip systems striking at high angles to the normal faults on the northern and southern ends of the rift (Fig. 2) (Strecker et al., 1995). Topographic relief attributed to extension and inferred uplift rates suggest that most

of the extension along the Karakul rift is Quaternary (Blisniuk and Strecker, 1996).

Several models have been proposed to explain the origin of east-west extension in the Pamir, which predict different variations in the distribution and timing of extension. Brunel et al. (1994) proposed that the Kongur Shan normal fault is the result of synorogenic extension, developing synchronously with motion along the Main Pamir Thrust in order to accommodate growth of topography along the Kongur Shan and Muztaghata gneiss domes. The model predicts initiation of extension and greatest magnitudes of extension to be along the Kongur Shan and Muztaghata gneiss domes at the center of the extensional system, with initiation age and magnitude of extension decreasing to the northern and southern ends of the fault system (Fig. 3A). Strecker et al. (1995) proposed that extension in the Pamir may be driven by radial thrusting of the Pamir salient along the Main Pamir thrust. This model predicts initiation of extension along the northern portion of the fault, propagating southward, with the greatest magnitude of extension along the northern portion of the fault (Fig. 3B). Alternatively, Yin et al. (2001) proposed that extension may be driven by oroclinal bending of the entire Pamir–western Himalayan region (Fig. 3C). Although mechanically different from the radial thrusting model, the predicted kinematic pattern of extension in the northern Pamir is the same. Additionally, it has been proposed that extension within the northern Pamir is due to northward propagation of the right-slip Karakoram fault (Ratschbacher et al., 1994; Strecker et al., 1995; Murphy et al., 2000). These models predict initiation of extension at the southern end of the Kongur Shan extensional system, propagating northward, with the greatest magnitude of extension along the southern portion of the fault system (Fig. 3D). It is also possible that east-west extension in the northern Pamir is part of the regional east-west extension in Tibet (Armijo et al., 1989) or eastern Asia (Yin, 2000). This interpretation implies that extension in the Pamir is coeval with other north-trending rifts in Tibet and eastern Asia. The results presented below, based on field and analytical studies along the northern portion of the Kongur Shan extensional system, allow us to begin to test the predictions of these competing models.

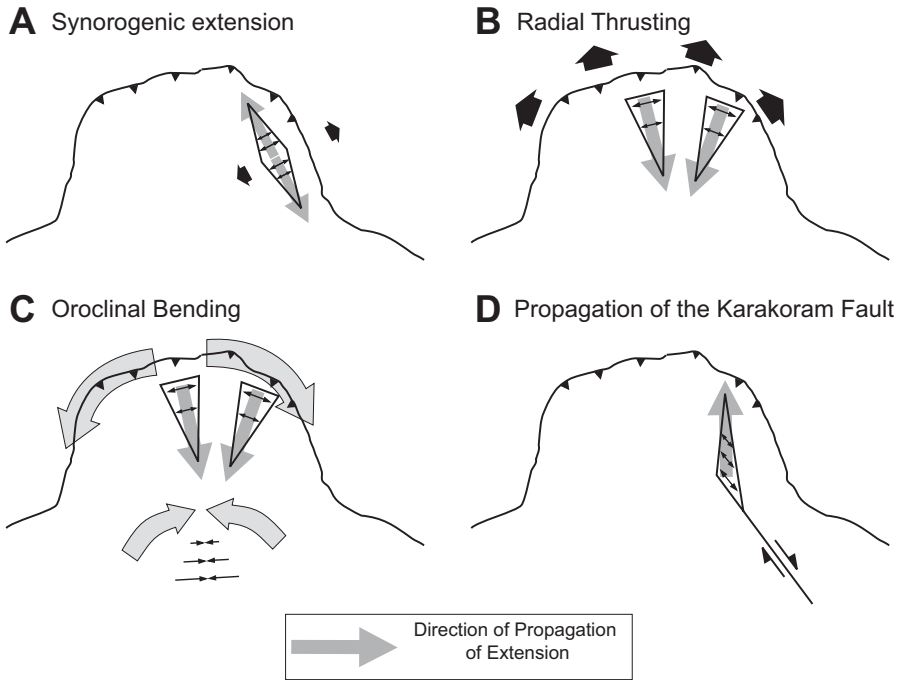

Figure 3. Models for the evolution of east-west extension in the Pamir. (A) Synorogenic extension related to motion along the Main Pamir thrust (Brunel et al., 1994). (B) Radial thrusting along the Main Pamir thrust (Strecker et al., 1995). (C) Oroclinal bending of the Pamir–western Himalayan region (Yin et al., 2001). (D) Northward propagation of the right-slip Karakoram fault (Ratschbacher et al., 1994; Strecker et al., 1995; Murphy et al., 2000).

KONGUR SHAN EXTENSIONAL SYSTEM

With local relief of over 4 km, the 250-km-long north-south–trending Muji-Tashkorgan Valley and its adjacent >7500 m peaks (Kongur Shan and Muztaghata) are some of the most prominent topographic features of the Pamir salient. The valley is bounded by faults of the Kongur Shan extensional system, which we divide into four main segments based on geometric and kinematic differences (Fig. 2). The northernmost segment is the 60-km-long, south-southwest–dipping Muji fault. Displacement along the Muji fault changes from right slip at its western end (Figs. 4A and 4B) to dominantly normal slip at its eastern end. At the eastern terminus of the Muji fault, the fault system changes abruptly from west-northwest–striking to north striking, becoming the Kongur Shan normal fault (Fig. 2). The Kongur Shan normal fault bounds the western flank of the mountain belt along the eastern side of the valley for ~150 km, dipping moderately (35°–45°) to the west and southwest (Figs. 4C and 4D). Field observations and interpretation of satellite images indicate normal slip, with little or no strike-slip component. Offset along the Kongur Shan normal fault dies out ~45 km south of the peak of Muztaghata, and extension is transferred to the east-dipping Tashkorgan normal fault via the 20-km-long, steeply west-northwest–dipping Tahman normal fault (Fig. 2). The Tashkorgan normal fault continues south for ~50 km, bounding the western side of the Tashkorgan Valley (Fig. 2). Field observations and interpretation of satellite images indicate that normal slip along the Tashkorgan normal fault decreases to the south. Mountains to the west of the city of Tashkorgan have well-defined triangular facets bounded by the Tashkorgan fault, whereas farther south topography is subdued, with no obvious expression of the fault (Figs. 4E and 4F). Additionally, the topographic relief of the western side of the valley also decreases southward, where the trace of the Tashkorgan fault becomes obscured.

PETROLOGY

The hanging wall and footwall of the northern portion of the Kongur Shan extensional system consist of medium- to high-grade metamorphic rocks. Petrologic studies were carried out in order to determine metamorphic mineral assemblages, trends in metamorphic grade, and deformation fabrics and kinematic indicators.

Electron microprobe analyses were obtained from selected samples to constrain peak pressure-temperature conditions (GSA data repository).[1] Analyses were obtained using a

[1]GSA Data Repository item 2004107, mineral composition and $^{40}Ar/^{39}Ar$ isotopic data, is available on the Web at http://www.geosociety.org/pubs/ft2004.htm. Requests may also be sent to editing@geosociety.org.

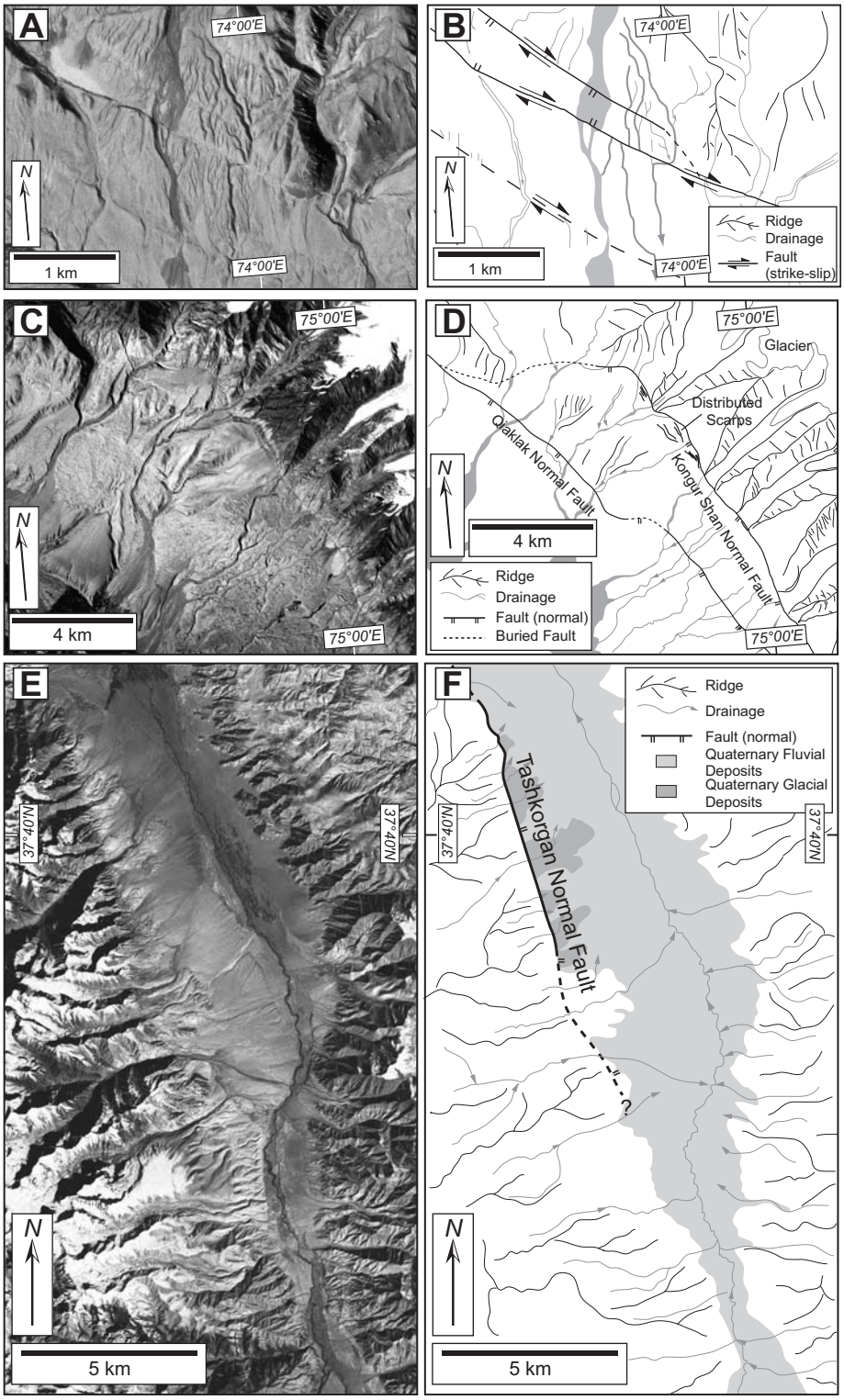

Figure 4. (A and B) CORONA image and interpretation of the western portion of the Muji fault segment at the western tip of the Muji Valley. Offset drainages (bold gray lines) show right-lateral sense of displacement. (C and D) CORONA image and interpretation of active fault scarps along the Kongur Shan fault segment to the north of the Kongur Shan massif. Smaller fault scarps of the Qiaklak fault are visible in Quaternary deposits west of the main fault trace. (E and F) Landsat image and interpretation of the Tashkorgan fault. The western range front is bounded by the fault to the north with well-defined triangular facets, while to the south, topography is subdued with no clear trace of the fault.

1 μm spot size (5 μm spot size for plagioclase analyses) with a 15 kV accelerating voltage, a 1.5×10^{-8} beam current, and a 20 second counting time for each element. Activities of phases and equilibrium Clapeyron slopes of exchange and net-transfer reactions were calculated using the programs AX and THERMOCALC 2.7 (Powell et al., 1998). Element maps and electron microprobe traverses were obtained to identify zoning patterns in garnets to interpret the pressure-temperature results.

Pressures and temperatures of equilibrium were calculated using the garnet-biotite exchange thermometer, and at least one of three net-transfer barometers: grossular + $2Al_2SiO_5$ + quartz = 3 anorthite (GASP) 3 anorthite + 6 ilmenite + 3 quartz = grossular + 2 almandine + 6 rutile (GRIPS) 3 ilmenite + 2 quartz + Al_2SiO_5 = almandine + 3 rutile (GRAIL) Metamorphic temperatures were obtained from garnet-biotite pairs using rim analyses (within the outer 10–20 microns) of garnet and analyses of biotite grains adjacent to garnet analyses. As analyses of plagioclase, ilmenite, and rutile did not show significant variation in composition, GASP, GRIPS, and GRAIL results were obtained using mean plagioclase, rutile, and ilmenite compositions with individual garnet analyses. Quartz and aluminosilicate phases were assumed to be pure.

Hanging Wall

The hanging wall of the Kongur Shan extensional system is composed of two lithologic units: (1) a structurally higher metasedimentary unit, Pz_{sch1}, which is intruded by granitic bodies, and (2) a structurally lower metagraywacke unit, Pz_{gw1} (Figs. 5A and 5B). Pz_{sch1} consists of medium- to high-grade metapelitic schists interlayered with micaceous quartzite, and minor amphibolite and marble. Petrologic studies indicate that the unit is part of a low-pressure, medium- to high-temperature Buchan metamorphic terrane, with a pronounced eastward increase in metamorphic grade (Fig. 6). Metapelites at the northwestern portion of the hanging wall, 15 km east of the town of Muji, are greenschist-facies biotite-chlorite schists. Metamorphic grade increases to the east with the successive appearance of andalusite, staurolite, garnet, sillimanite, and culminating in the appearance of K-feldspar, indicating upper-amphibolite- to granulite-facies metamorphic conditions. Garnets within the K-feldspar–bearing region are zoned with increasing Fe/(Fe + Mg) toward the rim, interpreted to represent diffusion zoning, and indicate that thermobarometry results would not reflect peak metamorphic conditions. However, the presence of andalusite throughout much of the hanging

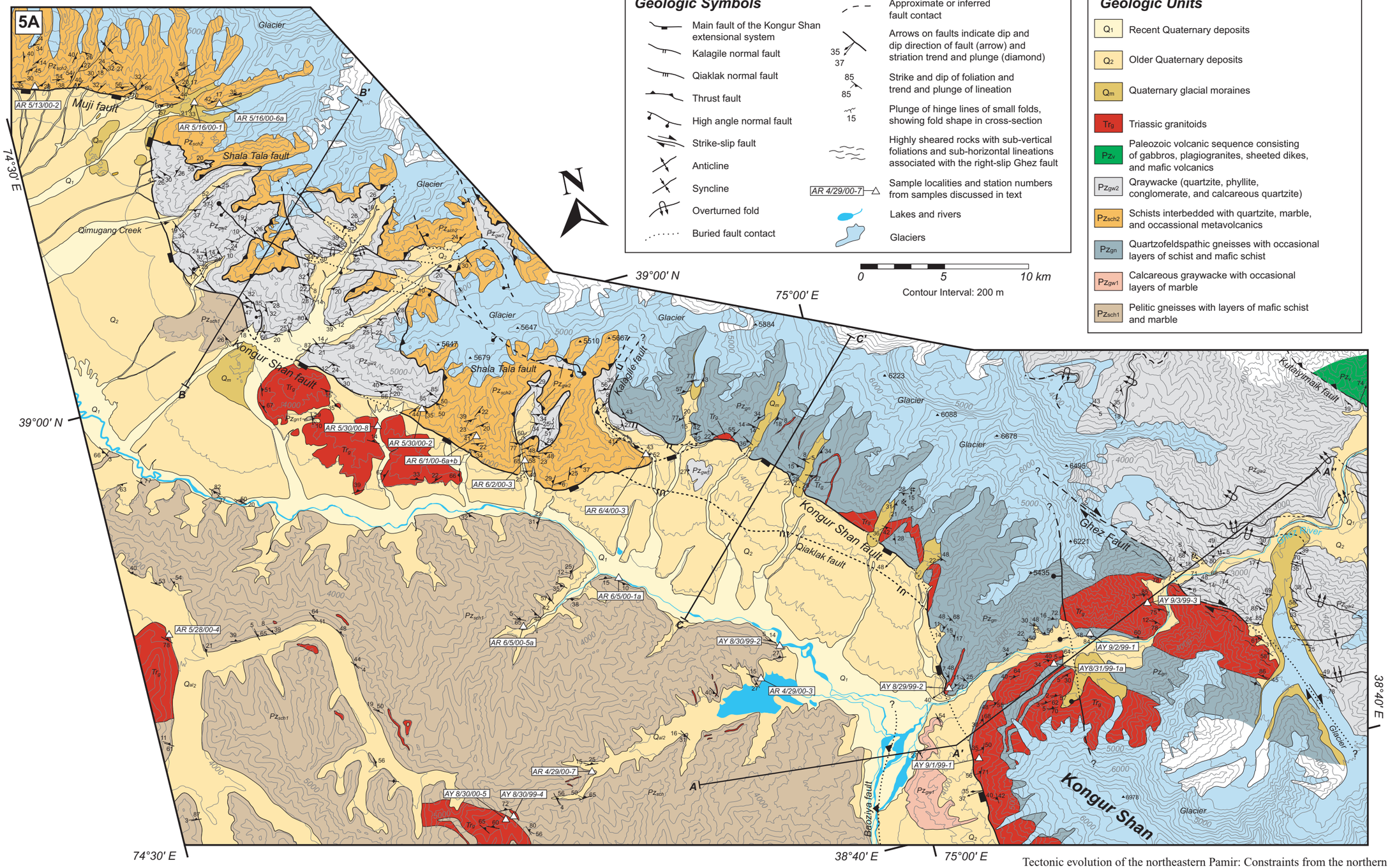

Geologic Symbols

- Main fault of the Kongur Shan extensional system
- Kalagile normal fault
- Qiaklak normal fault
- Thrust fault
- High angle normal fault
- Strike-slip fault
- Anticline
- Syncline
- Overturned fold
- Buried fault contact
- Approximate or inferred fault contact
- Arrows on faults indicate dip and dip direction of fault (arrow) and striation trend and plunge (diamond) (35 / 37)
- Strike and dip of foliation and trend and plunge of lineation (85 / 85)
- Plunge of hinge lines of small folds, showing fold shape in cross-section (15)
- Highly sheared rocks with sub-vertical foliations and sub-horizontal lineations associated with the right-slip Ghez fault
- Sample localities and station numbers from samples discussed in text (AR 4/29/00-7)
- Lakes and rivers
- Glaciers

Geologic Units

- Q_1 Recent Quaternary deposits
- Q_2 Older Quaternary deposits
- Q_m Quaternary glacial moraines
- Tr_g Triassic granitoids
- PZ_v Paleozoic volcanic sequence consisting of gabbros, plagiogranites, sheeted dikes, and mafic volcanics
- PZ_{gw2} Qraywacke (quartzite, phyllite, conglomerate, and calcareous quartzite)
- PZ_{sch2} Schists interbedded with quartzite, marble, and occassional metavolcanics
- PZ_{gn} Quartzofeldspathic gneisses with occasional layers of schist and mafic schist
- PZ_{gw1} Calcareous graywacke with occasional layers of marble
- PZ_{sch1} Pelitic gneisses with layers of mafic schist and marble

Figure 5. (A) Geologic map of the northern portion of the Kongur Shan extensional system (see text for B, C, and D).

Tectonic evolution of the northeastern Pamir: Constraints from the northern portion of the Cenozoic Kongur Shan extensional system, western China
Alexander C. Robinson et al.
Figure 5A
Supplement to *Geological Society of America Bulletin*, v. 116, no. 7/8

wall restricts peak pressures in those regions to <4 kbar. The transition directly from andalusite grade to sillimanite grade with no kyanite also suggests that the sillimanite-grade portion of the hanging wall was at similarly low pressures. Metamorphic K-feldspar, assuming the presence is related to crossing the second sillimanite isograd, suggests minimum peak metamorphic temperatures of ~650–700 °C for the inferred pressures of 4–5 kbar along the eastern portion of the hanging wall (Spear and Cheney, 1989).

The structurally lower metagraywacke unit, Pz_{gw1}, is exposed directly west of the Kongur Shan massif (Fig. 5A), as well as farther south, northwest of the Muztaghata massif. It consists of light gray-green calcareous quartzites and dark gray slates, with minor layers of marble and amphibolite. Typical assemblages are quartz + white mica + calcite ± plagioclase ± chlorite, indicating greenschist-facies metamorphic conditions.

Footwall

Muji Fault and Qimugang Creek Area

The footwall of the Muji fault and northwestern portion of the Kongur Shan normal fault footwall are composed of two main lithologic units: (1) a structurally higher heterogeneous metasedimentary unit, Pz_{sch}, exposed along the Muji fault and the Qimugang Creek portion of the Kongur Shan fault (Fig. 5A), and (2) a structurally lower metagraywacke unit, Pz_{gw}, exposed along the Qimugang Creek portion of the Kongur Shan fault (Fig. 5A).

Pz_{sch2} can be divided into two subunits based on compositional variations, the transition between which is gradational and not shown on Figure 5A. The structurally higher subunit is exposed within the footwall of the Muji fault and consists of calcareous quartzite, marble, and micaceous quartzite, with minor layers of pelitic schist and mafic metavolcanics. Schist layers are heavily retrograded, with chlorite replacement of biotite, garnet, and staurolite. Retrograde alteration decreases progressively to the east and south, with schist layers preserving amphibolite-facies assemblages of sillimanite + garnet at the juncture of the Muji and Kongur Shan faults. The structurally lower subunit is exposed along the Qimugang Creek portion of the Kongur Shan normal fault and is less compositionally heterogeneous, consisting of pelitic schists and micaceous quartzite, with infrequent thin layers of marble and metavolcanics. Schists are garnet-kyanite–bearing, consistent with this subunit being a structurally deeper portion of Pz_{sch2}.

[2]Figure 5A is on a separate sheet accompanying this issue.

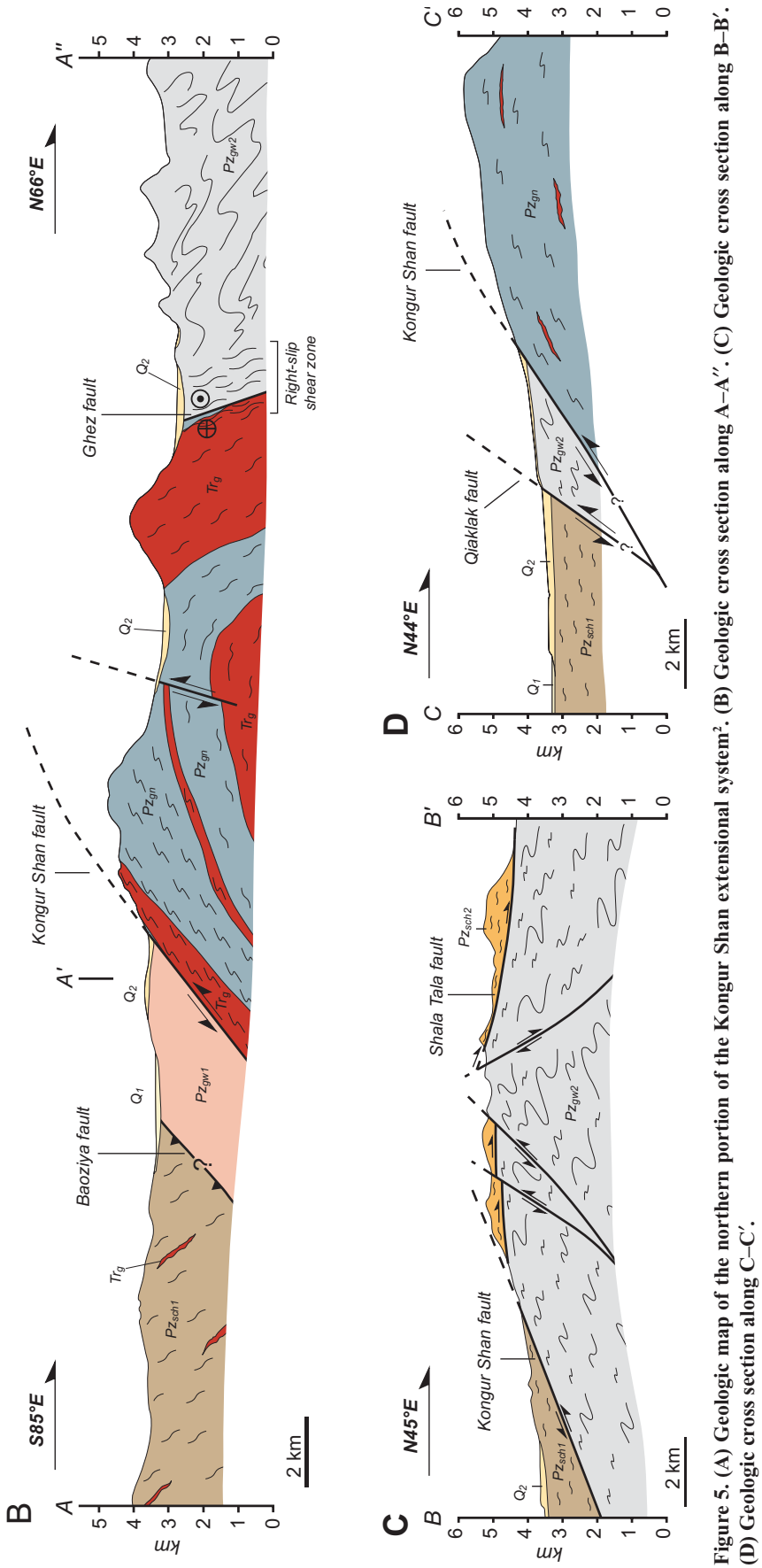

Figure 5. (A) Geologic map of the northern portion of the Kongur Shan extensional system[2]. (B) Geologic cross section along A–A″. (C) Geologic cross section along B–B′. (D) Geologic cross section along C–C′.

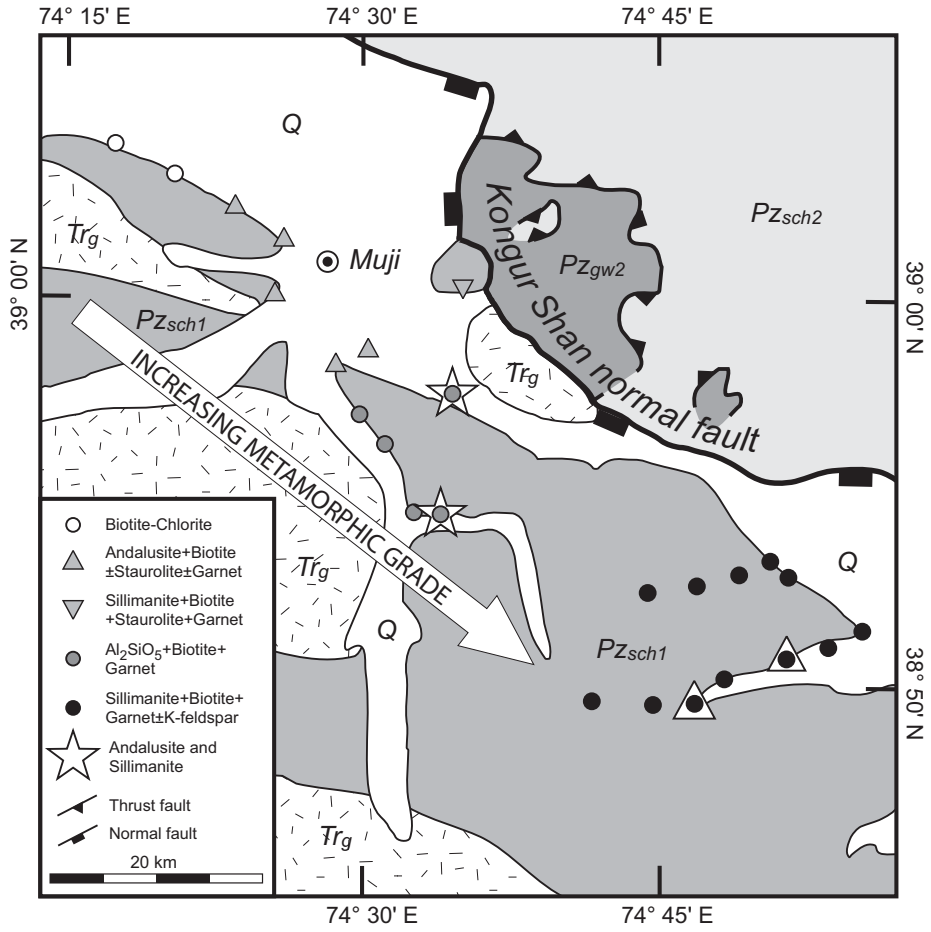

Figure 6. Simplified geologic map of the northern portion of the hanging wall of the Kongur Shan extensional system showing the sample locations and key mineral assemblages from each sample locality. Metamorphic grade increases from west to east, from biotite-chlorite grade to K-feldspar-sillimanite grade. Lithologic units are the same as in Figure 5.

Peak metamorphic conditions were determined from two garnet-kyanite–bearing schists, AR5/30/00-2 and AR6/2/00-3b, along the Qimugang Creek portion of the Kongur Shan fault (Figs. 5A and 7A). Garnets from both samples show significant compositional zoning (Fig. 8), with decreasing Fe/(Fe + Mg) toward the rim, indicating growth zoning. Pressure-temperature conditions were calculated using the garnet-biotite geothermometer and GRAIL, GASP, and GRIPS geobarometers, with both samples yielding peak metamorphic conditions of 8–9 kbar and 600–700 °C (Fig. 9).

Footwall metagraywacke unit Pz_{gw2} consists of fine- to medium-grained red to beige metagraywacke and calcareous metagraywacke, with infrequent layers of coarse metaconglomerate. Metaconglomerate layers contain matrix-supported clasts of marble and graywacke. Typical mineral assemblages for the fine- and medium-grained metagraywacke are quartz + plagioclase + smectite ± calcite with trace opaque minerals (Fig. 7B), indicating low-grade metamorphic conditions.

Kongur Shan Massif

Footwall rocks of the Kongur Shan massif are composed of medium-grained quartzofeldspathic mylonitic gneisses with minor layers of quartz-rich schist and biotite schist (Pz_{gn2}, Figures 5A and 5B). Pelitic schist layers within the Kongur Shan gneisses along the Ghez river contain garnet + kyanite ± staurolite, indicating amphibolite-facies metamorphic conditions. Minor retrograde replacement of biotite by chlorite is common. North of the Ghez river, quartzofeldspathic mylonitic gneisses of the

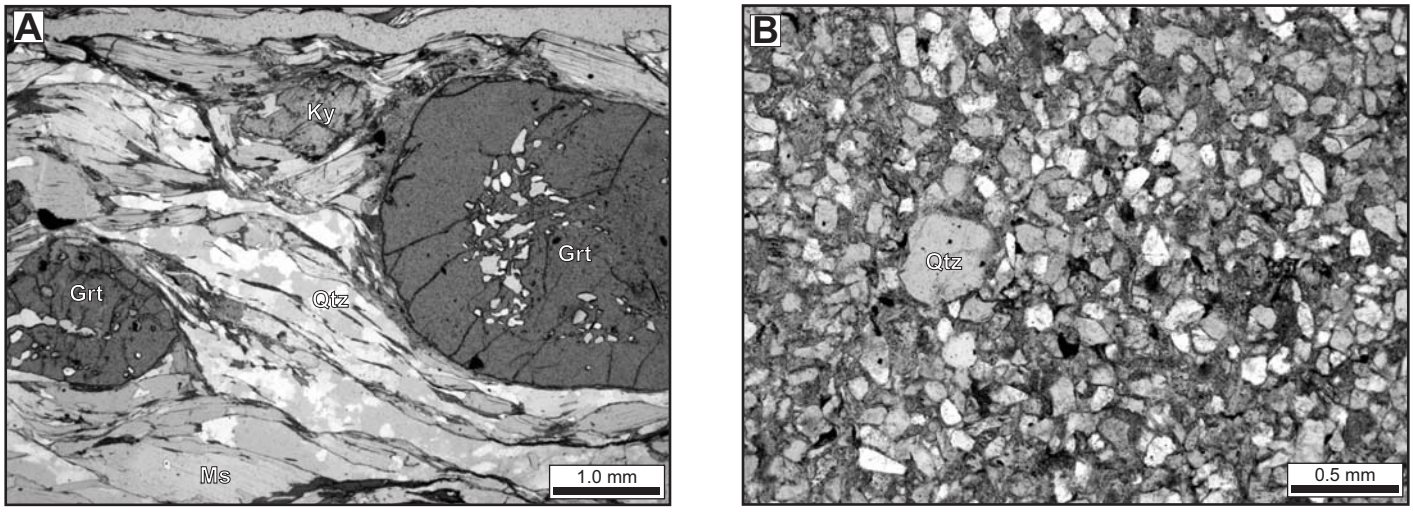

Figure 7. Photomicrographs of amphibolite-facies schist from the footwall unit Pz_{sch2} (A), and low-grade metagraywacke from footwall unit Pz_{gw2} (B) along the northern portion of the Kongur Shan fault segment.

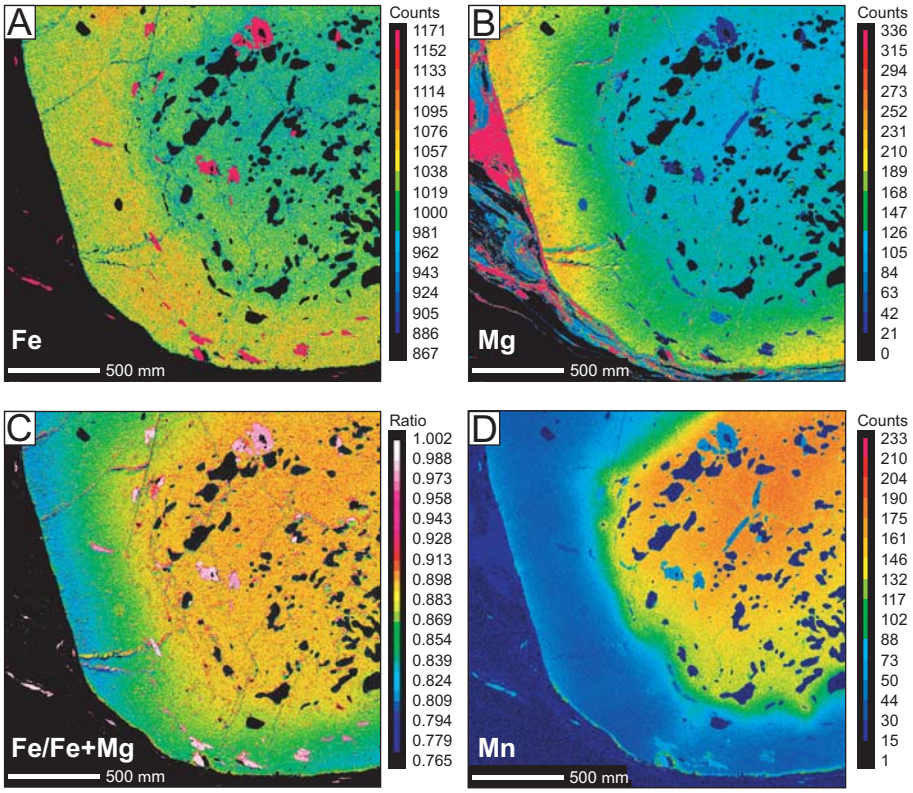

Figure 8. Element maps of a garnet from schist sample AR6/2/00-3b from the upper unit along the northern portion of the footwall. The garnets show significant chemical zoning with decreasing Fe (A), increasing Mg (B), and decreasing Fe/(Fe + Mg) (C) and Mn (D), interpreted to indicate growth zoning.

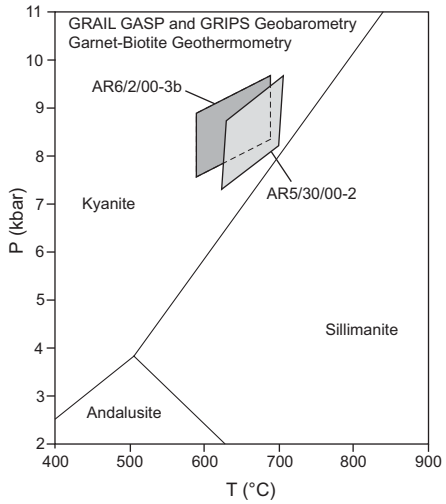

Figure 9. Thermobarometry results from footwall schists from footwall unit Pz_{sch2} indicating peak metamorphic conditions of 8–9 kbar and 600–700 °C. Boxes show regions where the different thermobarometers intersect.

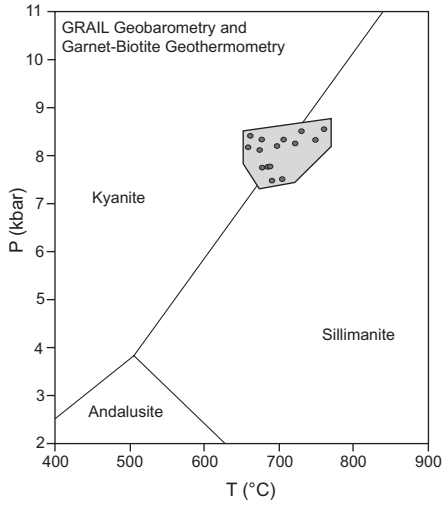

Figure 10. Thermobarometry results from footwall schists along the Kongur Shan massif indicating peak metamorphic conditions of ~8.5 kbar, 650–750 °C. Boxes bracket the region where the different thermobarometers intersect. Circles within the box are where garnet-biotite pairs and GRAIL analyses using the garnet analysis from the thermometry intersect.

massif grade into mylonitic calcareous quartzites, schistose quartzites, and mafic schists.

Analytical results to determine peak metamorphic conditions were obtained from sample AY8/29/99-2, a garnet-kyanite-staurolite–bearing schist (with staurolite occurring as inclusions in the garnet) located along the western flank of the Kongur Shan massif directly below the surface of the fault (Fig. 5A). Garnet from sample AY8/29/99-2 is compositionally zoned, with decreasing Fe/(Fe + Mg) toward the rims, indicating preservation of growth zoning. Results from the GRAIL barometer and garnet-biotite thermometer yield pressure-temperature conditions of ~8 kbar, 650–750 °C (Fig. 10). The presence of kyanite and absence of sillimanite suggest that the higher-temperature portions of the data may not correspond to peak equilibrium conditions due to minor retrograde reactions. Alternatively, the sample may have passed from the kyanite to the sillimanite stability field without growing sillimanite during isobaric heating at peak pressures. Our analytical results indicate higher grade of metamorphism for the Kongur Shan gneisses than that cited by Brunel et al. (1994) of 5–6 kbar and 500 °C from samples of the same composition (garnet-kyanite-staurolite–bearing schists). However, as the source of their estimates is not given, the origin of the discrepancy cannot be evaluated.

Twenty kilometers east of the range front, mylonitic gneisses (Pz_{gn}) are separated from a unit of massive beige to light-red metagraywacke (Pz_{gw2}) by the right-slip Ghez fault (Figs. 5A and 5B). The metagraywacke (Pz_{gw2}) is dominated by thick (hundreds of meters) layers of micaceous quartzite and minor layers of phyllite (quartz ± muscovite ± chlorite ± biotite). All exposures of metagraywacke within the footwall of the Kongur Shan normal fault are considered part of the same lithologic unit, Pz_{gw2}, based on lithologic similarities. The presence of biotite in Pz_{gw2} east of the Kongur Shan massif suggests higher metamorphic conditions than along the Qimugang Creek area. Finally, although similar in metamorphic grade to hanging-wall metagraywacke Pz_{gw1}, differences in color, higher amounts of carbonate, and the abundance of interbedded marbles and dark gray slates all suggest Pz_{gw1} is a lithologically distinct unit from Pz_{gw2}.

Plutonic Bodies

Igneous bodies along the northern portion of the Kongur Shan extensional system are identified as Late Permian to early Mesozoic

in age (Pan, 1992, 1996) (Tr_g, Fig. 5A). They are correlated with plutons of the Late Paleozoic–early Mesozoic South Kunlun terrane (Pan, 1992, 1996; Youngun and Hsu, 1994; Matte et al., 1996), which yield dominantly Triassic to Early Jurassic U-Pb zircon ages (Pan, 1992, 1996; Matte et al., 1996; Cowgill et al., 2003).

Igneous intrusions within the hanging wall consist primarily of several large granitic bodies (tens of square kilometers in areal extent) within unit Pz_{sch1} (Figs. 2 and 5A). Biotite granites are unfoliated to weakly foliated and found within the lower-grade portion of unit Pz_{sch1} (andalusite-grade and lower, Figure 6). Biotite-hornblende granites are weakly to moderately foliated and found within the higher-grade portion of unit Pz_{sch1}. Small pegmatitic dikes (tens of centimeters to several meters), veins, and pods also occur within Pz_{sch1}, with variable mineral compositions of quartz + plagioclase + tourmaline ± K-feldspar ± biotite ± muscovite ± garnet. Pegmatitic bodies are unfoliated, intrude subparallel to foliation within the metasedimentary units and crosscut the larger granitic plutons.

Within the footwall, large (>1 km thick) granitic sills with well-developed mylonitic fabrics are interlayered with Pz_{gn}, forming the core of the Kongur Shan massif (Figs. 5A and 5B). North of the Ghez river, smaller (≤100 m thick) granitic sills are found within Pz_{gn}, becoming less abundant farther north. Igneous bodies are rare within Pz_{sch2}, consisting of small veins and dikes of granitic composition. No igneous bodies were observed within either metagraywacke unit (Pz_{gw1} or Pz_{gw2}).

STRUCTURAL GEOLOGY

Hanging-Wall Structures

Metamorphic rocks from hanging-wall unit Pz_{sch1} have been pervasively ductilely deformed. Foliations in the metasedimentary rocks have a consistent northwest strike with moderate to steep dips and variable dip direction. Stretching lineations are common, defined by elongated quartz rods, and trend northwest with shallow to subhorizontal plunges. Schists generally have well-developed shear fabrics, with kinematic indicators such as rotated porphyroclasts, inclusion trails, and S-C shear fabrics showing right-slip sense of shear. Based on these observations, hanging-wall schists are interpreted to have been part of a right-slip ductile shear zone. Deformation appears to have occurred synchronously with or prior to peak metamorphic conditions, as evidenced by spiral inclusion patterns in garnet and staurolite and by small fibrolite mats overprinting foliation, respectively.

The contact between the hanging-wall schists (Pz_{sch1}) and hanging-wall metagraywacke unit (Pz_{gw1}) is the Baoziya fault (Figs. 5A and 5B). Where exposed along the Karakoram Highway south of the Kongur Shan massif, the fault dips moderately (~25°) to the west-northwest and carries high-grade schists of Pz_{sch1} in its hanging wall, separated from metagraywacke unit Pz_{gw1} in its footwall by an ~1-m-thick gouge zone. Shear fabrics in the gouge zone and underlying metagraywacke indicate top-to-the-south sense of shear (Pan, 1992, and our own field observations). The juxtaposition of high-grade rocks over low-grade rocks indicates that the Baoziya fault is a south-directed thrust.

Footwall Structures

Along the western flank of the Kongur Shan massif, the Kongur Shan normal fault dips ~30°–45° to the west and is commonly associated with a 20–40-m-thick zone of chloritic breccia within the footwall. Structurally below the fault surface, gneisses, schists, and plutonic rocks are strongly mylonitized, with west-plunging mineral lineations (Fig. 5A) and S-C mylonitic fabrics indicating top-to-the-west shear (Fig. 11A) (Brunel et al., 1994, and our own field observations). Along the Ghez river, footwall foliations within Pz_{gn} and the granitic sills define a structural dome (Brunel et al., 1994), with dip directions varying systematically from west to east as one moves eastward into the footwall. Mylonitic lineations also rotate clockwise toward the east near the Ghez fault, from a westerly trend to a northerly trend (Fig. 5A).

Although the Kongur Shan normal fault was not directly observed south of the junction with the Muji fault, two lines of evidence suggest that the dip of the fault is significantly shallower there than along the Kongur Shan massif to the south. (1) Assuming the fault is relatively planar, projection of the topographic expression of the trace of the fault ~5 km south of Qimugang Creek onto a cross section indicates that the fault surface dips ~20° to the west-southwest (cross section B–B′, Fig. 5C). (2) The topographic slope of the footwall along Qimugang Creek, where not incised, dips 17°–18° to the west and appears to be very planar (Fig. 11B). We interpret this slope to be the exhumed fault zone, implying an ~20° dipping fault.

Northwest of the Kongur Shan massif and west of the main range-bounding Kongur Shan fault is the Qiaklak fault (Figs. 5A and 5C). The Qiaklak fault is expressed as a linear escarpment in Quaternary sediments in the Muji Valley with apparent down-to-the-west normal offset (Figs. 4C and 4D), and has outcrops of metagraywacke unit Pz_{gw2} within the northwest portion of its footwall. Both ends of the Qiaklak fault merge with, or are truncated by, the Kongur Shan normal fault (Fig. 5A).

North of the Qiaklak fault, mafic schists of Pz_{gn} are separated from metagraywacke unit Pz_{gw2} by the Kalagile fault (Fig. 5A). The contact between the two units is not exposed but is overlain by a zone of heavily faulted metagraywacke (Pz_{gw2}) with numerous gouge zones, which dip steeply (60°–70°) to the west to northwest. Shear fabrics in the gouge zones within Pz_{gw2} show top-to-the-west sense of shear, indicating normal sense of displacement along the fault. The southeastern tip of the Kalagile fault appears to merge with the Kongur Shan normal fault.

Along the eastern flank of the Kongur Shan massif, mylonitic gneisses (Pz_{gn}) and granites are juxtaposed against lower-grade metagraywacke unit Pz_{gw2} across the north-northwest–striking Ghez fault of Brunel et al. (1994) (Figs. 5A and 5B). Where exposed, the fault dips steeply (70°–80°) to the east, with a thin (10–15 cm) gouge zone. Rocks for several kilometers on either side of the fault are ductilely sheared, with subvertical foliations striking to the north-northwest, and subhorizontal mineral stretching lineations. Kinematic indicators (rotated porphyroclasts and S-C shear fabrics) within the shear zone in both the mylonitic gneisses and metagraywacke show right-slip sense of shear.

East of the Ghez fault, metagraywacke of unit Pz_{gw2} is deformed by large northeast-vergent overturned to upright isoclinal folds (amplitudes of >1 km) (Fig. 5A). Map-scale fold axes trend west-northwest and are truncated by the Ghez fault. Smaller-scale folds with similar orientations and amplitudes of several centimeters are observed at the outcrop scale. Folding style of Pz_{gw2} along the Qimugang Creek portion of the footwall is similar to that observed east of the Kongur Shan massif, with large northwest-trending overturned isoclinal folds (amplitudes of >1 km). Smaller northwest-trending asymmetric folds (amplitude of several centimeters) and en echelon quartz veins (Fig. 10C) are common in Pz_{gw2}, with both showing top-to-the-north-northeast sense of shear.

Along the Muji fault, footwall unit Pz_{sch2} is deformed by large east-northeast–trending upright, tight to open folds with amplitudes of ≤1 km and wavelengths of ~500 m to >1 km (Figs. 5A and 11D). Large folds within Pz_{sch2} are not observed along the Kongur Shan normal fault, with only outcrop-scale northeast-vergent overturned folds. Near the contact between footwall units Pz_{sch2} and Pz_{gw2}, schists of Pz_{sch2} are ductilely sheared with northeast-trending mineral-stretching lineations and kinematic indicators (rotated porphyroblasts, mica fish,

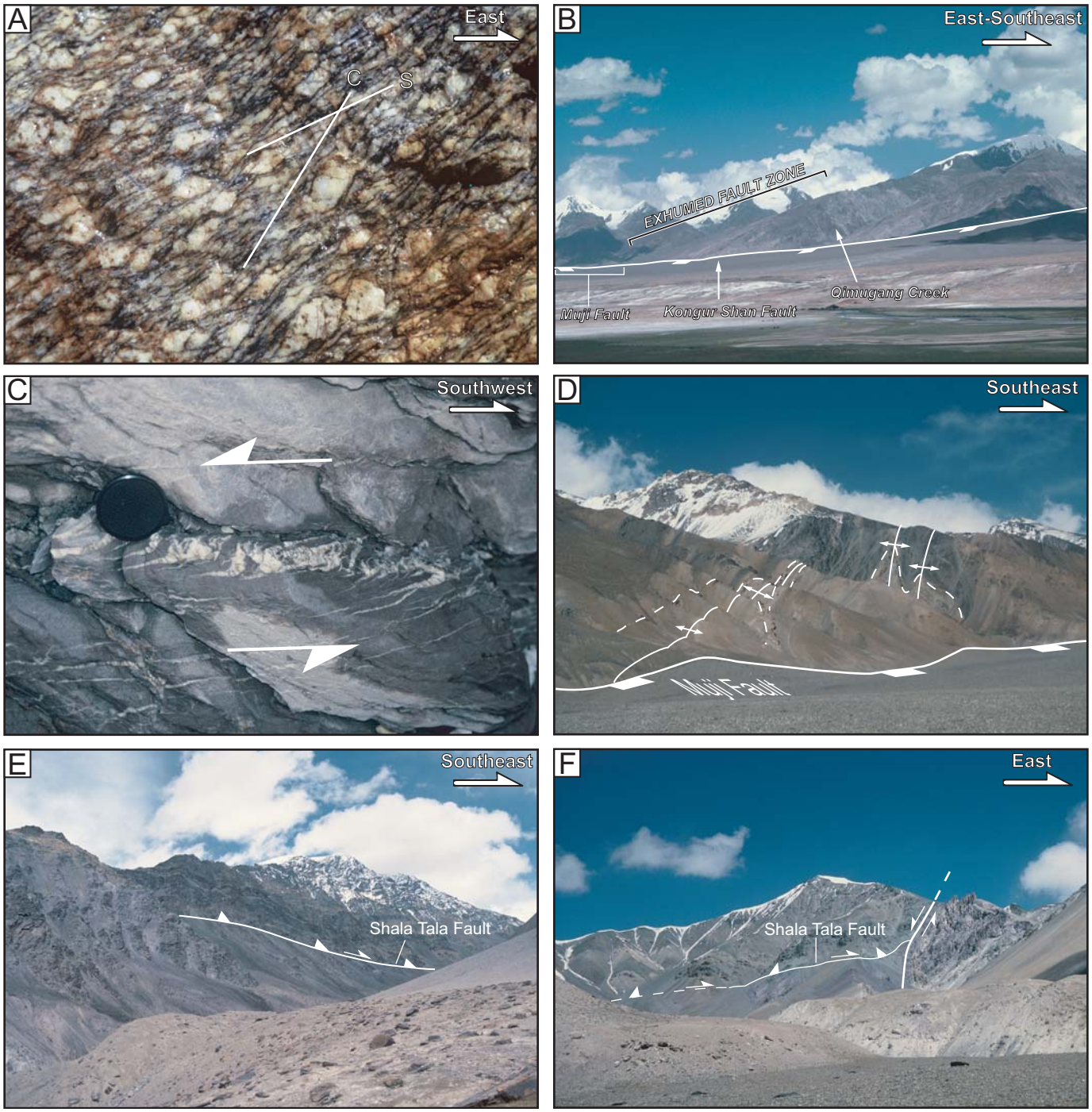

Figure 11. (A) Field photo of S-C mylonitic fabric in footwall gneisses of the Kongur Shan massif immediately below the fault surface. Photo is to the north, with shear indicators showing top-to-the-west sense of shear. Field of view is ~15 cm across. (B) Field photo looking north-northwest from the town of Muji at the footwall of the Qimugang Creek portion of the Kongur Shan fault. The active fault lies along the base of the mountain. The planar, low topographic grade of the western flank of the mountain is interpreted to be the exhumed fault surface. (C) Tension gashes in footwall metagraywacke unit Pz_{gw2} showing top-to-the-northeast sense of shear. Photo is to the southeast. Lense cap (6 cm) for scale. (D) Isoclinal folds deforming schists and marble in footwall unit Pz_{sch2} along eastern portion of the Muji fault. Photo is to the northeast. (E) Field photo looking to the northeast at the head of the Qimugang Valley. The upper unit is amphibolite-facies schists of Pz_{sch2}, and the lower unit is low-grade metagraywacke of Pz_{gw2}. The subhorizontal contact between the units is the north-northeast–directed Shala Tala thrust. Photo is to the northeast. (F) High-angle fault (bold line) cutting the Shala Tala thrust. Sense of motion on the high-angle fault is interpreted to be normal. Photo is to the northwest.

and occasional S-C tectonite fabrics) showing top-to-the-northeast sense of shear.

Schists of unit Pz_{sch2} are separated from the structurally lower metagraywacke (Pz_{gw2}) by the Shala Tala fault (Figs. 5A and 5C). Where exposed, the fault is defined by a gouge zone (<1 m to ~10 m thick) with a low to moderate dip angle and variable dip direction (Fig. 11E). The juxtaposition of higher-grade over lower-grade rocks indicates the Shala Tala fault is a thrust. Shear fabrics in the gouge zone of the fault indicate top-to-the-north or top-to-the-northeast sense of shear, consistent with kinematic indicators within both Pz_{sch1} and Pz_{gw1}. The variable dip direction indicates that the fault may have been subsequently folded.

In the Qimugang Creek area, northwest-striking high-angle faults cut the Shala Tala thrust (Figs. 5A, 5C, and 11F). As they strike subparallel with the active Kongur Shan normal fault, they are interpreted to be normal faults, related to recent east-west extension. The magnitude of displacement across these faults is unknown due to a lack of marker beds in unit Pz_{gw2}.

U-Pb ZIRCON GEOCHRONOLOGY

U-Pb Methods

Zircons were obtained from two samples using standard rock-crushing and mineral separation techniques, mounted in epoxy with zircon standard AS3 (age 1099.1 Ma, Paces and Miller, 1993) and Au coated. U-Pb analyses were obtained with the University of California at Los Angeles (UCLA) CAMECA ims 1270 ion microprobe using an O^- primary beam of ~10 nA focused to an ~15 × 20 µm spot. U-Pb ratios were determined by using a calibration curve based on UO/U versus Pb/U determined from the zircon standard. Isotope ratios were corrected for common lead based on a ^{204}Pb correction using the model of Stacey and Kramers (1975).

U-Pb Results

Sample AR5/28/00-4 is a weakly foliated biotite granite in hanging-wall unit Pz_{sch1} located ~15 km south-southeast of the town of Muji (Fig. 5A). Seven zircons were analyzed (Fig. 12A; Table 1). Five analyses yielded results that lie on or just above concordia and form a cluster with a weighted mean $^{206}Pb/^{238}U$ age of 217 ± 3 Ma (MSWD = 0.64), interpreted to be the age of the granite. Two zircons yielded discordant analyses that lie along a chord between the interpreted emplacement age and an upper intercept of ca. 1150 Ma.

Sample AY9/3/99-3 is a biotite-hornblende mylonitic granite sill from the footwall of the Kongur Shan normal fault ~15 km east of the range front along the Ghez river (Fig. 5A). Eleven analyses were obtained from nine zircon grains (Fig. 12B; Table 1). Results define a spread of generally concordant ages from 260 to 186 Ma, with all but one analysis falling between 215 and 260 Ma. We interpret these ages to indicate mixing between two age domains within the zircons, an older core and a younger rim. This interpretation is supported by results from a zircon that yielded a rim $^{206}Pb/^{238}U$ age of 221 ± 9 Ma and a core $^{206}Pb/^{238}U$ age of 245 ± 5 Ma. The rims of the zircon are characterized by oscillatory magmatic zoning and thus are unlikely to represent metamorphic overgrowths. The age of the granite is interpreted to be represented by the younger ages (220–230 Ma), with the youngest age the result of resetting during a later thermal event.

Th-Pb MONAZITE GEOCHRONOLOGY

In situ Th-Pb ages were obtained for monazite grains occurring as inclusions in garnet from each of the three high-grade metamorphic units (Pz_{sch1}, Pz_{sch2}, and Pz_{gn}, Fig. 5A). As garnet appears at slightly higher metamorphic conditions than monazite in most pelitic compositions during prograde metamorphism (Wing et al., 2003), monazite inclusions can be interpreted to date metamorphic events associated with garnet growth (Harrison et al., 1997; Catlos et al., 2002) as a result of either sluggish kinetics (Cherniak et al., 2004; cf. Smith and Giletti, 1997) or shielding from subsequent lead loss by the garnet (Montel et al., 2000).

Th-Pb Methods

Monazite grains occurring as inclusions in garnet and within the matrix of samples

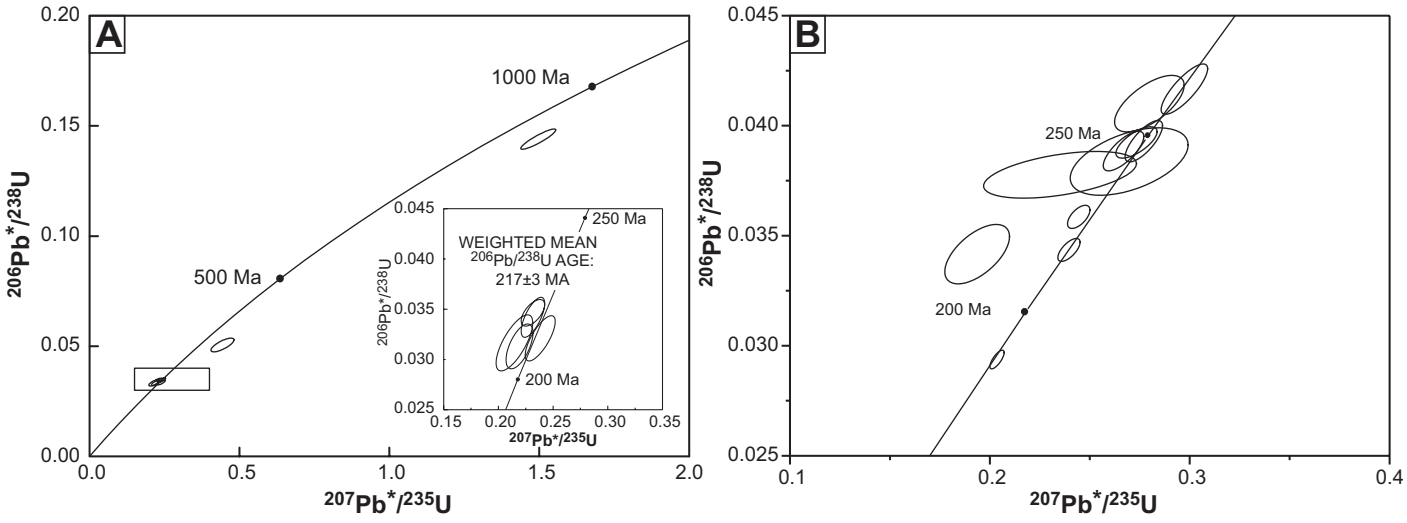

Figure 12. Concordia plots of individual ion microprobe analyses of zircons from granites of the Kongur Shan extensional system. Error ellipses are 1σ. (A) Results from sample AR5/28/02-4 yield five concordant analyses that form a cluster with a weighted mean $^{206}Pb/^{238}U$ age of 217 ± 3 Ma, interpreted to be the age of the granite. Two discordant analyses lie along a chord with an upper intercept of ca. 1150 Ma. (B) Results from sample AY9/3/99-3 yield a spread of generally concordant analyses from ca. 260 to 180 Ma. The older ages are generally from the cores of zircons, while most rim ages fall at 220–230 Ma. The age of the granite is interpreted to be Middle Triassic.

TABLE 1. ZIRCON U-Pb ISOTOPIC DATA

Spot ID†	Isotopic ratios							Ages ± 1 s.e.		
	$^{206}Pb^*/^{238}U$	± 1 s.e.	$^{207}Pb^*/^{235}U$	± 1 s.e.‡	$^{207}Pb^*/^{206}Pb$	± 1 s.e.‡	$^{206}Pb^*$ (%)	$^{206}Pb^*/^{238}U$	$^{207}Pb^*/^{235}U$	$^{207}Pb^*/^{206}Pb$
AY9/3/99-3										
8, 1	3.78E-02	1.06E-03	2.35E-01	3.83E-02	4.52E-02	6.83E-03	92.98	239.0 ± 6.6	214.4 ± 31.4	negative
10, 1	2.94E-02	4.24E-04	2.04E-01	3.57E-03	5.03E-02	5.89E-04	99.71	186.6 ± 2.7	188.2 ± 3.0	207.2 ± 27.2
4, 1	3.59E-02	5.26E-04	2.45E-01	5.61E-03	4.94E-02	9.13E-04	99.62	227.1 ± 3.3	222.1 ± 4.6	168.9 ± 43.1
4, 2	3.44E-02	5.21E-04	2.40E-01	5.56E-03	5.06E-02	8.75E-04	99.33	217.8 ± 3.2	218.1 ± 4.6	221.6 ± 40.0
3, 1	3.84E-02	1.53E-03	2.70E-01	2.95E-02	5.10E-02	4.91E-03	98.85	242.7 ± 9.5	242.5 ± 23.6	239.8 ± 222.1
24, 1	4.10E-02	1.28E-03	2.80E-01	1.74E-02	4.95E-02	2.39E-03	99.33	259.1 ± 8.0	250.5 ± 13.8	171.2 ± 112.6
22, 1	4.17E-02	1.15E-03	2.97E-01	1.16E-02	5.18E-02	1.20E-03	99.26	263.1 ± 7.1	264.3 ± 9.0	274.8 ± 53.22
15, 1	3.93E-02	9.40E-04	2.77E-01	9.37E-03	5.11E-02	1.14E-03	99.74	248.5 ± 5.8	248.3 ± 7.5	246.8 ± 51.52
21, 1	3.42E-02	1.35E-03	1.94E-01	1.62E-02	4.11E-02	2.80E-03	99.07	216.6 ± 8.4	179.7 ± 13.8	negative
21, 2	3.89E-02	9.00E-04	2.67E-01	1.02E-02	4.98E-02	1.30E-03	99.55	245.7 ± 5.6	240.2 ± 8.1	186.8 ± 60.89
23, 1	3.92E-02	7.13E-04	2.73E-01	1.03E-02	5.05E-02	1.44E-03	99.49	248.1 ± 4.4	245.4 ± 8.2	219.3 ± 65.74
AR5/28/00-4										
40, 1	3.36E-02	1.14E-03	2.38E-01	1.38E-02	5.15E-02	2.04E-03	99.64	212.8 ± 7.1	217.0 ± 11.3	263.0 ± 90.7
25, 1	5.06E-02	3.14E-03	4.44E-01	3.85E-02	6.36E-02	3.67E-03	100	317.9 ± 19.2	372.7 ± 27.1	728.9 ± 122.2
26, 1	3.32E-02	1.12E-03	2.19E-01	1.24E-02	4.80E-02	2.15E-03	99.64	210.3 ± 7.0	201.4 ± 10.3	97.9 ± 105.8
23, 1	1.44E-01	4.63E-03	1.50E+00	5.86E-02	7.54E-02	1.27E-03	100	867.8 ± 26.0	929.5 ± 23.8	1079.0 ± 33.67
24, 1	3.33E-02	1.40E-03	2.15E-01	1.68E-02	4.67E-02	2.62E-03	99.16	211.4 ± 8.8	197.5 ± 14.1	34.38 ± 134.3
28, 1	3.49E-02	6.67E-04	2.32E-01	1.08E-02	4.82E-02	1.83E-03	99.42	220.8 ± 4.2	211.6 ± 8.87	110.3 ± 89.59
22, 1	3.46E-02	1.00E-03	2.40E-01	1.36E-02	5.03E-02	2.13E-03	99.34	219.4 ± 8.2	218.6 ± 11.2	209.3 ± 97.91

†Spot ID: #,# = zircon number, spot number.
*Radiogenic Pb corrected for common Pb with composition $^{206}Pb/^{204}Pb$ = 18.35, $^{207}Pb/^{204}Pb$ = 15.61, $^{208}Pb/^{204}Pb$ = 37.48 estimated from model of Stacey and Kramers (1975).
‡s.e.: standard error.

were located in polished thin sections using a scanning electron microscope (SEM) with an energy-dispersive spectrometer (EDS). Relevant portions of the thin sections were mounted in epoxy with several monazite standard grains (monazite standard 554 with an age of 45 ± 1 Ma; Harrison et al., 1999) and Au coated. Th-Pb analyses were obtained in situ using similar conditions to the zircon analyses, except that Th-Pb ratios were determined using a calibration curve of ThO_2/Th versus Pb/Th determined from the standard.

Hanging Wall

Sample AR4/29/00-3a is a garnet-sillimanite–bearing schist located in the high-grade, K-feldspar–bearing portion of the hanging-wall unit Pz_{sch1} (Fig. 5A). Thirteen monazite grains were analyzed: ten from monazite inclusions in garnet and three from monazite within the matrix. $^{208}Pb/^{232}Th$ ages range from 235 to 195 Ma, with most analyses falling between 230 and 200 Ma (Fig. 13A; Table 2). Multiple monazite inclusions from single garnets yield a spread of ages with no discernable spatial pattern, and with the same distribution in ages from matrix monazites. These results are interpreted to indicate that garnet growth and peak metamorphic conditions in the hanging wall occurred during the Late Triassic between 200 and 230 Ma.

Footwall

Sample AR5/30/00-2, used in thermobarometric analyses of footwall unit Pz_{sch2}, was analyzed to date the timing of high-grade metamorphism

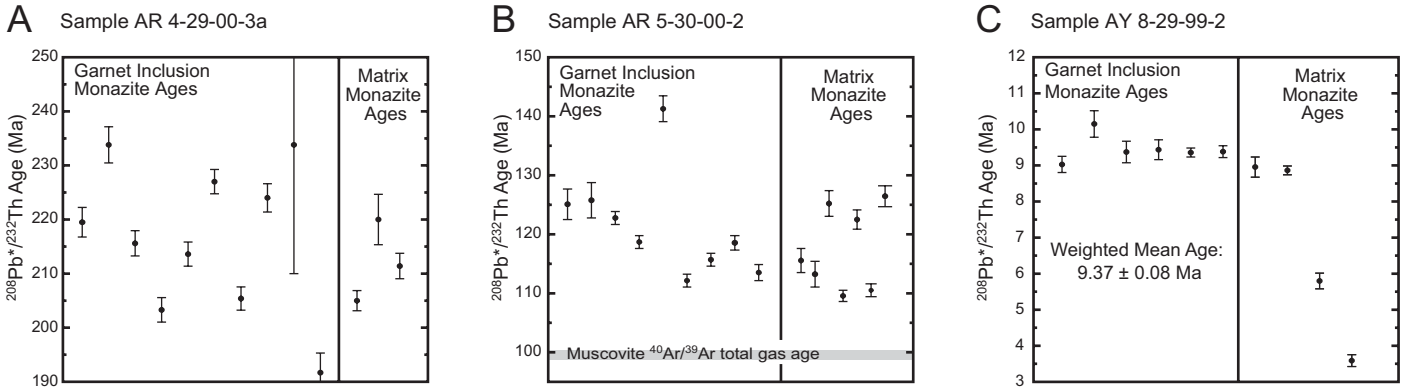

Figure 13. Results from in situ ion microprobe dating of monazite grains from different high-grade schists along the northern portion of the Kongur Shan extensional system. (A) Analyses from hanging-wall unit Pz_{sch1}, with a spread in both inclusion ages and matrix ages from 200 to 230 Ma interpreted to date timing of peak metamorphism. (B) Analyses from footwall unit Pz_{sch2}, with a spread in both inclusion ages and matrix ages from ca. 110 to 130 Ma interpreted to date timing of peak metamorphism. Horozontal gray line is the muscovite total gas age from the same sample. (C) Gneisses of the Kongur Shan massif showing inclusion ages with a weighted mean age of 9.37 ± 0.8 Ma interpreted to date the timing of peak metamorphism. Two analyses from the matrix yield the same age, while two others are significantly younger and are interpreted to be reset (see discussion in text). Error bars are ±1σ.

TABLE 2. MONAZITE Th-Pb ISOTOPE DATA.

Garnet	Grain	$^{208}Pb^*/^{232}Th$	± 1 s.e.	$^{208}Pb/^{204}Pb$	$^{208}Pb^*$ (%)	$^{208}Pb^*/^{232}Th$ age‡ (Ma ± 1 s.e.)
Sample AR4/29/00-3						
1	1	1.09E-02†	1.37E-04	3877	99.03	219.0 ± 2.7
1	2	1.16E-02†	1.68E-04	1838	97.96	233.8 ± 3.3
1	3	1.07E-02†	1.17E-04	7776	99.52	215.6 ± 2.3
3	1	1.01E-02†	1.13E-04	5708	99.34	203.3 ± 2.3
3	2	1.06E-02†	1.12E-04	6191	99.39	213.6 ± 2.2
3	3	1.13E-02†	1.12E-04	3249	98.85	227.0 ± 2.2
4	1	1.02E-02†	1.08E-04	3995	99.06	205.4 ± 2.1
4	2	1.12E-02†	1.31E-04	4649	99.19	224.0 ± 2.6
4	3	1.16E-02†	1.19E-03	11,320	99.67	233.8 ± 23.8
5	1	9.53E-03†	1.81E-04	8259	99.55	191.7 ± 3.6
matrix		1.02E-02†	9.30E-05	8342	99.55	205.0 ± 1.9
matrix		1.09E-02†	2.33E-04	5497	99.32	220.0 ± 4.7
matrix		1.05E-02†	1.18E-04	1920	98.05	211.4 ± 2.3
Sample AY8/29/99-2						
Inclusion	1	4.47E-04§	1.11E-05	130.8	70.57	9.0 ± 0.2
Inclusion	2	5.03E-04§	1.81E-05	151.1	74.53	10.2 ± 0.4
Inclusion	1	4.64E-04§	1.48E-05	119.8	67.85	9.4 ± 0.3
Inclusion	1	4.67E-04§	1.36E-05	127.6	69.83	9.4 ± 0.3
Inclusion	1	4.63E-04§	6.18E-06	187.7	79.49	9.4 ± 0.1
Inclusion	1	4.64E-04§	8.12E-06	172.9	77.73	9.4 ± 0.2
Matrix	1	4.43E-04§	1.38E-05	127.5	69.80	9.0 ± 0.3
Matrix	1	4.39E-04§	6.04E-06	200.0	80.75	8.9 ± 0.1
Matrix	2	2.87E-04§	1.08E-05	114.7	66.43	5.8 ± 0.2
Matrix	1	1.78E-04§	8.06E-06	98.0	60.71	3.6 ± 0.2
Sample AR5/30/00-2						
2	1	6.21E-03#	1.24E-04	3433	98.93	125.1 ± 2.5
2	2	6.24E-03#	1.45E-04	911.5	95.97	125.7 ± 3.0
3	1	6.10E-03#	5.43E-05	5767	99.35	122.8 ± 1.1
3	2	5.90E-03#	5.60E-05	4196	99.10	118.8 ± 1.1
7	1	7.02E-03#	1.12E-04	4990	99.26	141.3 ± 2.2
9	1	5.56E-03#	5.59E-05	2808	98.66	112.1 ± 1.1
9	2	5.74E-03#	5.52E-05	5059	99.25	115.6 ± 1.1
9	3	5.89E-03#	5.75E-05	2263	98.33	118.6 ± 1.2
11	1	5.64E-03#	6.88E-05	4691	99.20	113.6 ± 1.4
Matrix	1	5.73E-03#	1.05E-04	2955	98.76	115.5 ± 2.1
Matrix	3	5.61E-03#	1.05E-04	3716	99.01	113.2 ± 2.1
Matrix	4	6.22E-03#	1.10E-04	2179	98.32	125.3 ± 2.2
Matrix	5	5.43E-03#	4.79E-05	2506	98.50	109.5 ± 1.0
Matrix	6	6.08E-03#	8.20E-05	3599	98.95	122.5 ± 1.6
Matrix	7	5.48E-03#	4.94E-05	2316	98.37	110.5 ± 1.0
Matrix	10	6.27E-03#	8.62E-05	3423	98.90	126.4 ± 1.7

Note: s.e.—standard error.
*Radiogenic Pb corrected for common Pb.
†Calculated by assuming $^{208}Pb/^{204}Pb$ = 37.5.
‡Ages determined from calibration based on monazite standard 554.
§Calculated by assuming $^{208}Pb/^{204}Pb$ = 38.5.
#Calculated by assuming $^{208}Pb/^{204}Pb$ = 37.67.

in that unit (Fig. 5A). Sixteen monazite grains were analyzed: ten monazite inclusions in garnet and eight monazite grains within the matrix. Ages from monazite inclusions and the matrix yield $^{208}Pb/^{232}Th$ ages that range between 130 and 110 Ma, with one age of 142 Ma falling outside the distribution (Fig. 13B; Table 2). These results are interpreted to date high-grade metamorphism of footwall unit Pz_{sch2} as middle Cretaceous between 110 and 130 Ma.

Sample AY8/29/99-2, used in thermobarometric analyses of footwall unit Pz_{gn2}, was analyzed to date the timing of high-grade metamorphism of the Kongur Shan gneisses (Fig. 5A). Ten Th-Pb ages were obtained from eight monazite grains: six monazite inclusions within garnets and four analyses from monazite located in the matrix of the sample. All six analyses of monazite inclusions in garnet yielded Late Miocene $^{208}Pb/^{232}Th$ ages between 9 and 10 Ma with a weighted mean age of 9.37 ± 0.09 Ma (MSWD = 1.57) (Fig. 13C; Table 2). Two of the four matrix monazite analyses yielded ages of ca. 9 Ma, indistinguishable from the monazite inclusion ages. This age is interpreted to date the timing of garnet growth during high-grade metamorphism. Two other matrix analyses yielded younger ages of 5.8 Ma and 3.7 Ma, interpreted to be a result of recrystallization or dissolution/reprecipitation during uplift and mylonitization (Harrison et al., 2002). As a side note, these results provide a cautionary example for interpreting bulk monazite U-Pb ages in terms of metamorphic events.

THERMOCHRONOLOGY

$^{40}Ar/^{39}Ar$ Methods

Six to 7 mg of mica separates, and ~18 mg of K-feldspar, were obtained using standard mineral separation techniques and handpicked in order to further purify the separates. Mineral separates and sanidine flux monitors were irradiated at the Ford reactor, University of Michigan, and the McMaster reactor, McMaster University, for 45 hours and 15 hours, respectively in five different irradiations (designated UM98, UM101, UM104, UM105, and UM109). Two different sanidine standards were used during the course of the analyses to determine reactor neutron flux: Fish Canyon Tuff (27.8 Ma) (Cebula et al., 1986; Renne et al., 1994) and Taylor Creek Tuff (28.1 Ma) (Renne et al., 1998). After irradiation, samples were step-heated in a Ta crucible in a double vacuum furnace, and isotopic compositions of the released gas were determined using a gas-source automated mass spectrometer. Isotopic data were reduced using an in-house data reduction program, AGECAL. Age uncertainties are reported at the 1σ level and do not include uncertainties in J-Factor or decay constants (Figs. 14, 15, 16, and 17; GSA data repository).

Hanging Wall

Six muscovite samples and one biotite sample were analyzed from schists and granites within hanging-wall unit Pz_{gn1} (Fig. 5A). All the analyses yielded Middle to Late Jurassic total gas ages (Fig. 14; Table DR1) from 134 to 172 Ma, with most of the total gas ages falling between 155 and 165 Ma. Analyses also show significant age gradients over the first several temperature steps, with some samples increasing from <100 Ma to 150–160 Ma over the first 20%–30% of the gas released (i.e., sample AR6/5/00-1a). This variation in age is interpreted to be the result of diffusional loss of Ar from samples with a preserved age gradient (e.g., Grove and Bebout, 1995), and thus suggests that the hanging-wall schists cooled slowly through the mica closure temperature. Similar ages between schists, granites, and late pegmatite dikes indicate that all analyses represent cooling ages postdating igneous and metamorphic events.

Ghez River Transect

Five samples were analyzed from granites and gneisses from the same footwall transect along the Ghez river used by Arnaud et al. (1993) (Fig. 5A). $^{40}Ar/^{39}Ar$ age spectra from muscovite and biotite analyses are relatively flat, indicating rapid cooling (Fig. 15; Table DR1). Weighted mean gas ages are interpreted to best represent the timing of bulk closure for the sample, as the initial and final steps (~10% of the total gas released) of several samples yield significantly older ages.

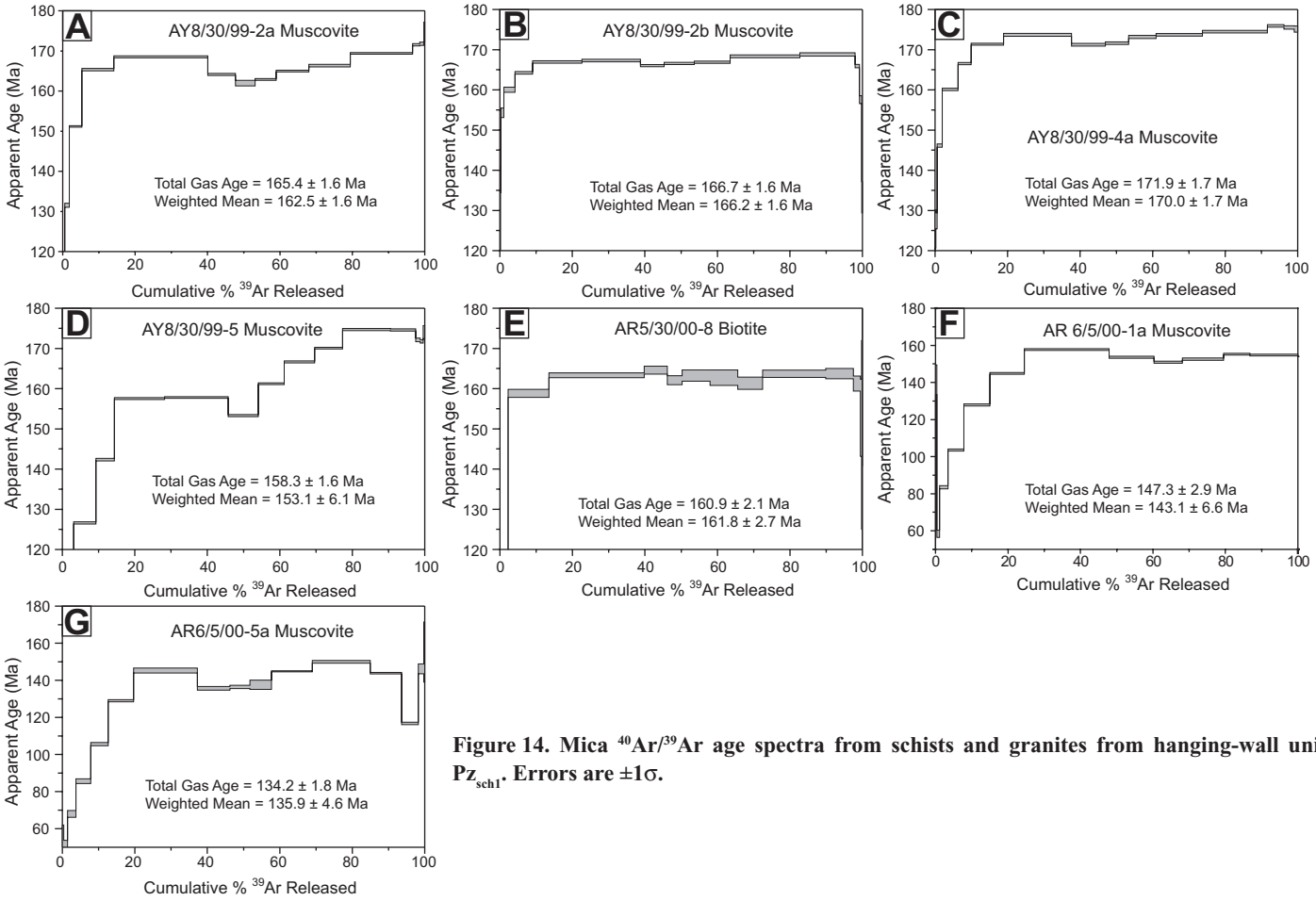

Figure 14. Mica $^{40}Ar/^{39}Ar$ age spectra from schists and granites from hanging-wall unit Pz_{sch1}. Errors are ±1σ.

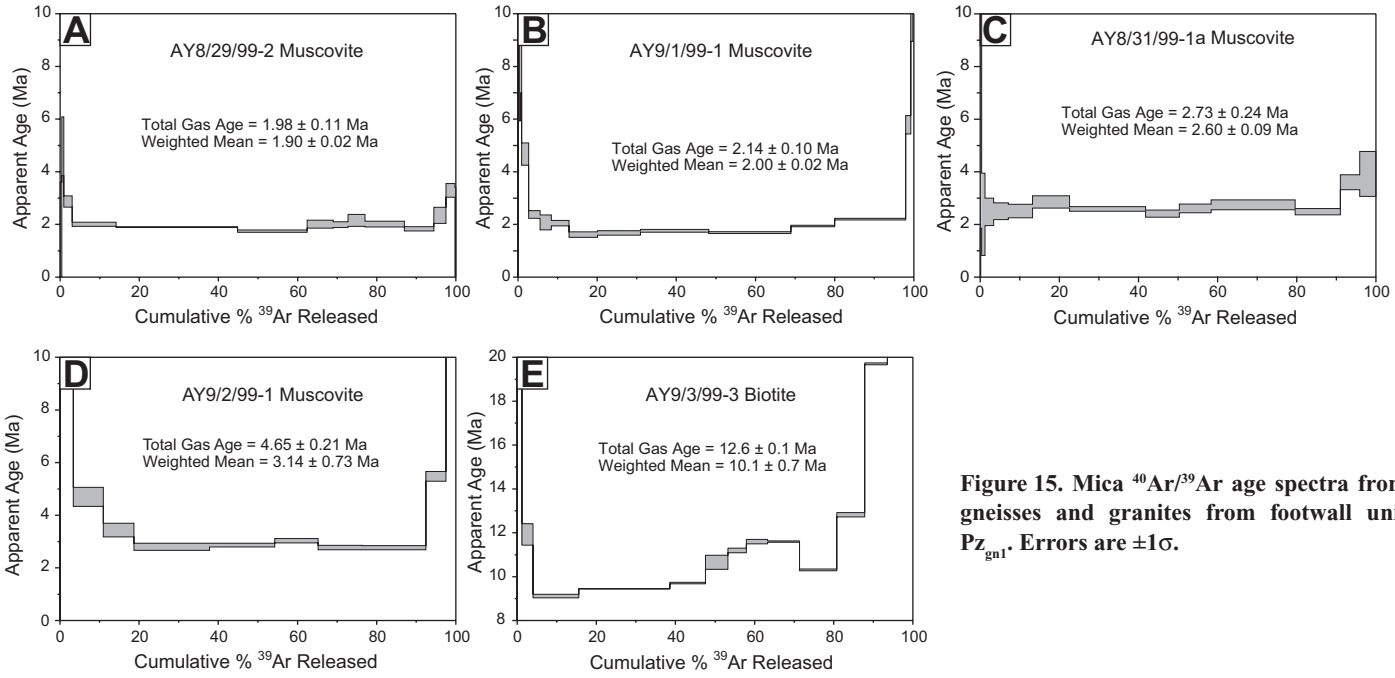

Figure 15. Mica $^{40}Ar/^{39}Ar$ age spectra from gneisses and granites from footwall unit Pz_{gn1}. Errors are ±1σ.

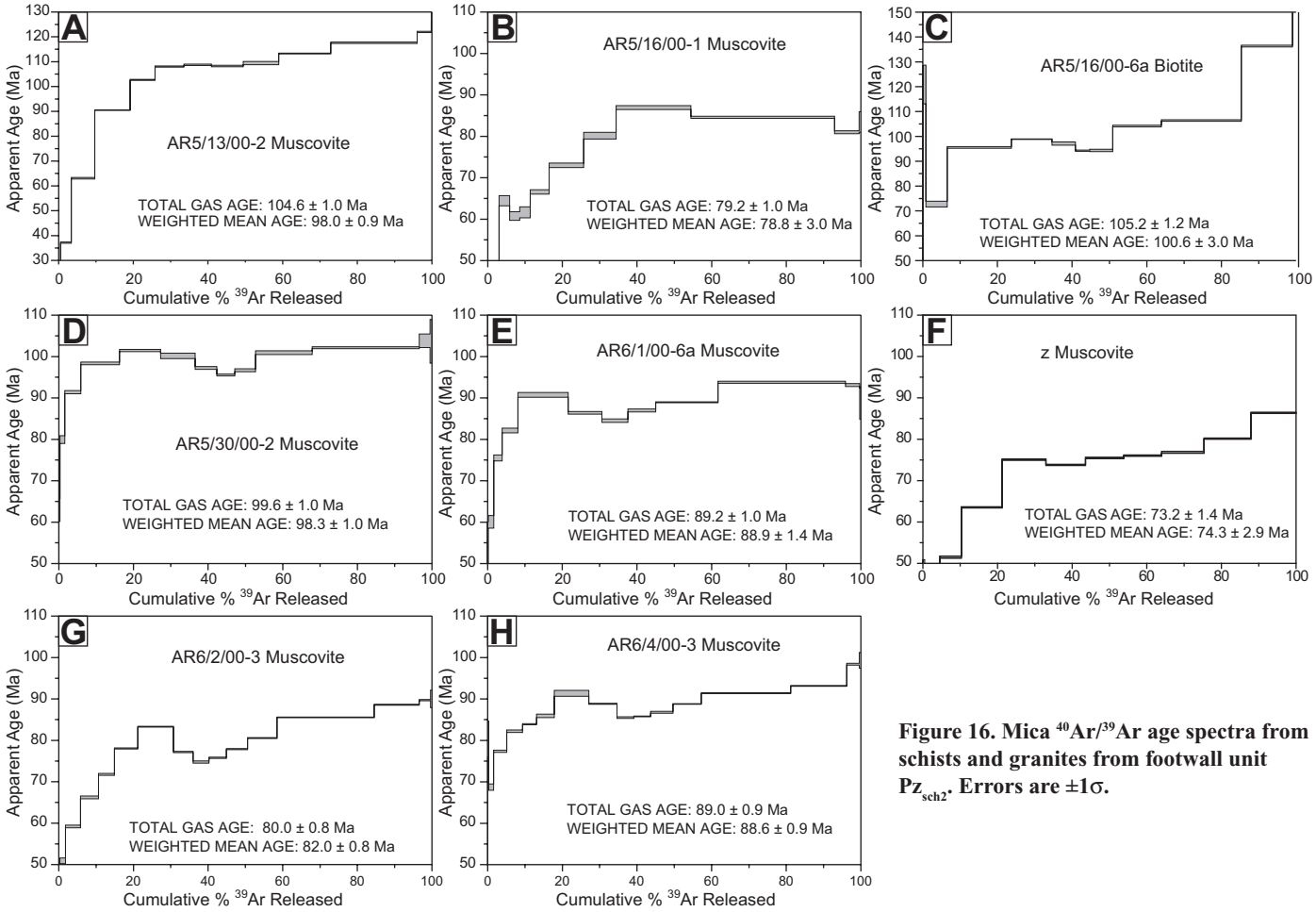

Figure 16. Mica $^{40}Ar/^{39}Ar$ age spectra from schists and granites from footwall unit Pz_{sch2}. Errors are ±1σ.

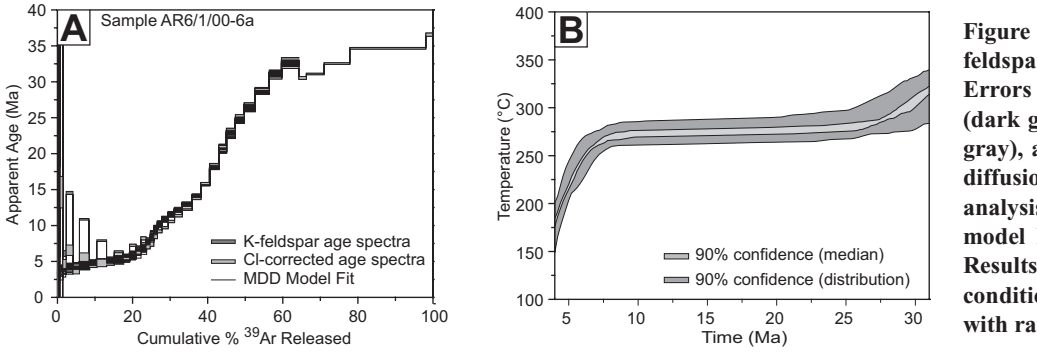

Figure 17. (A) Results from step-heating K-feldspar from footwall sample AR6/1/00-6a. Errors are ±1σ. Diagram shows age spectra (dark gray), Cl-corrected age spectra (light gray), and modeled fits (black) from multi-diffusion domain thermal modeling of the analysis. (B) Multidiffusion domain thermal model history for the K-feldspar analysis. Results indicate slow cooling to isothermal conditions throughout most of the Tertiary, with rapid cooling initiating at ca. 7–8 Ma.

Sample AY9/1/99-1 and AY8/29/99-2 are from the western flank of the Kongur Shan massif immediately below the fault surface and yield weighted mean muscovite ages of 2.00 ± 0.02 Ma and 1.90 ± 0.02 Ma, respectively (Figs. 5A, 15A, and 15B). Footwall ages increase to the east, from 2.60 ± 0.09 Ma ~6 km east of the fault (Figs. 5A and 15C), to 3.14 ± 0.73 Ma ~9 km east of the fault (Figs. 5A and 15D), to a biotite age of 10.11 ± 0.70 Ma 13 km east of the fault (Figs. 5A and 15E). These results are similar to those obtained by Arnaud et al. (1993).

Several K-feldspar separates were analyzed from samples of gneisses and deformed granites of the Kongur Shan massif. However, $^{40}Ar/^{39}Ar$ age spectra from these samples indicated significant amounts of excess ^{40}Ar, and no attempt to model the analyses was made. Additionally, K-feldspar age spectra used in multidiffusion domain (MDD) modeling by Arnaud et al. (1993) appear to be similarly affected by excess ^{40}Ar, suggesting that their modeling results (which indicated an increase in cooling rates at ca. 2 Ma) may not accurately represent the cooling history of the footwall.

Northern Footwall

Along the Muji fault and Qimugang Creek portion of the Kongur Shan normal fault, micas from eight samples were analyzed from Pz_{sch2} (Fig. 5A). Analyses are restricted to unit Pz_{sch2}, as the metagraywacke from unit Pz_{gw2} in this region lacks mineral assemblages suitable for $^{40}Ar/^{39}Ar$ analyses. Total gas and weighted mean ages are given on the $^{40}Ar/^{39}Ar$ age spectrum plots (Fig. 16; Table DR1). Although they commonly agree within error, the weighted mean age is interpreted as a more accurate indicator of the timing of bulk closure of the sample in analyses where it appears that an anomalous step (or steps) is significantly affecting the total gas age.

Along the eastern portion of the Muji fault segment (Fig. 5A), muscovite from samples AR5/13/00-2 and AR5/16/00-1 yielded total gas ages of 104.6 ± 1.0 Ma and 79.2 ± 1.0 Ma, respectively (Figs. 16A and 16B). A biotite analysis from sample AR5/16/00-6a yields a relatively flat age spectrum, with one anomalously old step at higher temperatures (Fig. 16C), and has a weighted mean age of 100.6 ± 3.0 Ma. Muscovite samples from the Qimugang creek portion of the Kongur Shan normal fault (Fig. 5A) yield a similar spread in ages from 74.3 ± 2.9 Ma (AR6/4/02-5b, Fig. 15F) to 98.3 ± 1.0 Ma (AR5/30/02-2, Fig. 16D), with most ages falling between 80 and 90 Ma. $^{40}Ar/^{39}Ar$ age spectra of most samples from Pz_{sch2} show a significant increase in age (ca. 20–40 Ma) over the first several steps (usually ~20% of the gas), with a saddle-shaped release spectra in the higher-temperature steps in several of the analyses. As with the hanging-wall analyses, the $^{40}Ar/^{39}Ar$ age spectrum is interpreted to indicate diffusional loss of Ar from samples with a preserved age gradient, indicating unit Pz_{sch2} was cooled slowly through the muscovite closure temperature. The saddle-shaped portion of the release spectrum is interpreted to reflect the micas structurally breaking down during step heating at the higher-temperature steps.

K-feldspar was analyzed from a granitic dike (sample AR6/1/00-6a, Fig. 5A) within Pz_{sch2}. Isothermal duplicates were run from temperatures of 400 to 800 °C in order to correct the age spectra for Cl-derived excess ^{40}Ar (Harrison et al., 1994). The Cl-corrected $^{40}Ar/^{39}Ar$ age spectra from the K-feldspar shows a relatively flat portion over the first 20%–25% of the gas with an age of 4–8 Ma (Fig. 17A; Table DR1), then increasing smoothly, peaking at ca. 35 Ma. Results from MDD modeling of the analysis (Lovera et al., 1997; Lovera et al., 2002) indicate slow cooling (or isothermal conditions) between 35 Ma and ca. 8 Ma, followed by rapid cooling from ~270 °C beginning at 7–8 Ma (Fig. 17B). These results support the inference from the muscovite analyses that the upper unit cooled slowly though the muscovite closure temperature.

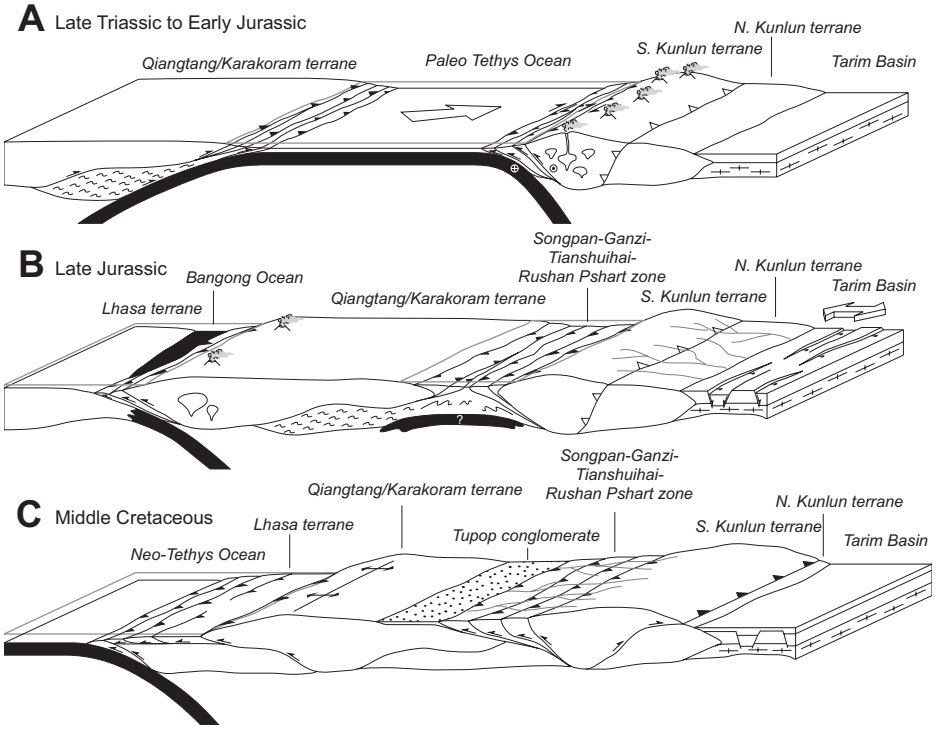

Figure 18. Mesozoic tectonic history of the Pamir–western syntaxis region. Open triangles indicate older Paleozoic suture zones. (A) Triassic northward subduction of the Paleo-Tethys ocean results in the development of an arc terrane along the southern margin of the Asian continent, with emplacement of granitic plutons and the development of a Buchan metamorphic terrane. Right-slip shear within the metasedimentary rocks is interpreted to be due to oblique subduction, as proposed by Mattern et al. (1996). (B) Jurassic mica ages in the hanging wall record slow cooling, synchronous with (but not necessarily related to) normal faulting and sedimentation in the Tarim basin (Sobel, 1999). (C) Middle Cretaceous crustal thickening and shortening occur along the northern margin of the Pamir, synchronous with metamorphic and igneous activity within the Karakoram terrane. These events are interpreted to be a result of the middle Cretaceous collision of the Lhasa block with the southern margin of Asia (Matte et al., 1996), and subsequent underthrusting of the Lhasa terrane beneath the Qiangtang terrane (e.g., Kapp et al., 2003).

DISCUSSION

Triassic

Petrologic studies of hanging-wall unit Pz_{sch1} of the Kongur Shan extensional system indicate it is part of a medium- to high-temperature, low-pressure Buchan metamorphic sequence. Th-Pb ages from monazite inclusions in garnet date this metamorphic event as Late Triassic to Early Jurassic (230–200 Ma), overlapping with U-Pb zircon ages from two large granites analyzed in this study, as well as U-Pb zircon ages of granites from previous studies in the region (Pan, 1992, 1996; Arnaud et al., 1993; Cowgill et al., 2003). The synchronous development of the Buchan metamorphic sequence and intrusion of granitic bodies suggests a Triassic–Early Jurassic arc setting for the hanging-wall lithologies (Fig. 18A). These results support the interpretation that the northern hanging wall of the Kongur Shan extensional system is an along-strike equivalent of the South Kunlun terrane, which developed during Permian to Early Jurassic north-directed subduction of the Paleo-Tethys ocean (Pan, 1992, 1996; Youngun and Hsu, 1994; Matte et al., 1996; Şengör and Natal'in, 1996; Xiao et al., 2002a, 2002b).

Hanging-wall schists from unit Pz_{sch1} also experienced pervasive right-slip ductile shear. Although Pan (1992) attributed right-slip shear within the hanging wall to Cenozoic motion on the right-slip Karakoram fault to the south, our results indicate that the hanging-wall deformation

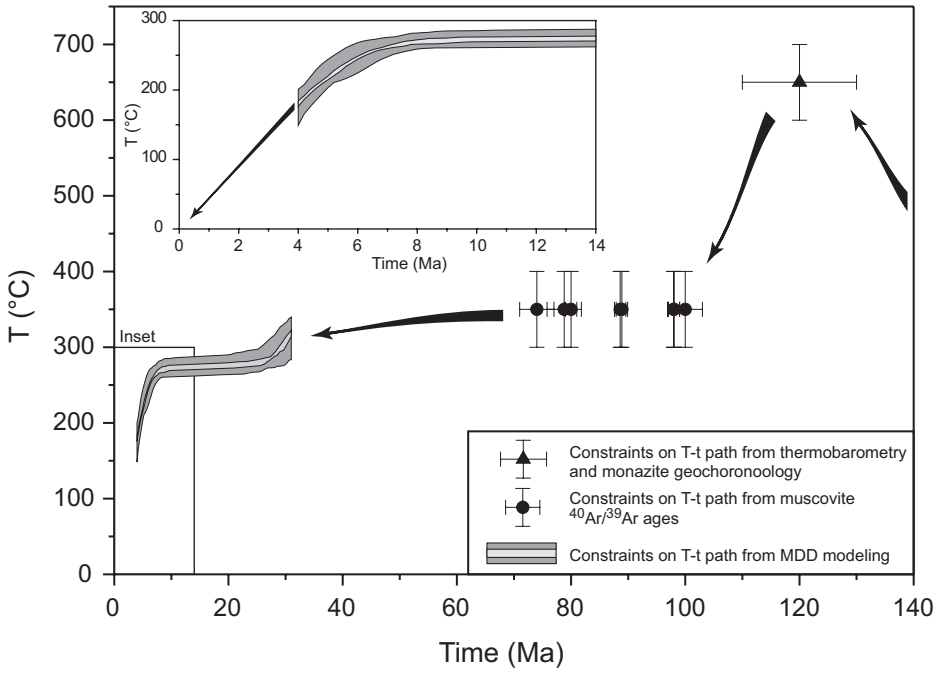

Figure 19. Temperature-time path of the schists from the northern portion of the footwall of the Kongur Shan extensional system, integrating results from *P-T* analyses and Th-Pb dating of monazite (triangle), $^{40}Ar/^{39}Ar$ dating of micas (circles), and multidiffusion domain modeling of a K-feldspar analysis (model from Fig. 17). The temperature-time path shows two periods of rapid cooling: one in the middle Cretaceous between peak metamorphic conditions and the mica cooling ages, and another beginning in the Late Miocene. Extrapolation of the MDD model results from 7 to 4 Ma (inset) suggests little change in cooling rates since initiation of extension.

is synchronous with metamorphic and igneous activity and is therefore Triassic in age. Right-slip ductile shear synchronous with Triassic pluton emplacement has previously been identified to the east along the South Kunlun suture by Mattern and Schneider (2000), who interpreted the shear to have developed within the active arc from oblique subduction of the Paleo-Tethys ocean. Our results provide further evidence in support of this hypothesis (Fig. 18A).

Jurassic

$^{40}Ar/^{39}Ar$ analyses of muscovite and biotite from schists and granites within hanging-wall unit Pz_{sch1} yield Middle to Late Jurassic cooling ages, with all but one of the ages falling between 160 and 170 Ma. Previous studies have found significant late Middle to Late Jurassic tectonic activity to the northeast in the Tarim basin, with detrital apatite fission track ages recording denudation and erosion synchronous with deposition of thick sedimentary sequences between ca. 165 and 145 Ma (Sobel and Dumitru, 1997; Sobel, 1999) (Fig. 18B). Similar signatures from studies around the Tarim basin and Qaidam basin also indicate widespread cooling and denudation during the Jurassic (Hendrix et al., 1992; Cowgill et al., 2001; Sobel et al., 2001; Yin et al., 2002). However, age spectra from the analyses indicating possible slow cooling suggest that the cooling ages are not the result of tectonic-related denudation. Although the Jurassic ages may have been related to motion on the Baoziya thrust, a likely alternative is that the Jurassic cooling was induced by thermal reequilibration of the crust after peak metamorphism associated with magmatism.

Cretaceous

Th-Pb monazite geochronology, thermobarometry, and $^{40}Ar/^{39}Ar$ thermochronology results from the hanging wall of the Shala Tala thrust indicate significant crustal thickening and shortening during the middle Cretaceous in the northeastern Pamir. Th-Pb ages of monazite inclusions in garnet and thermobarometric analyses show that footwall unit Pz_{sch2} was buried to mid-crustal conditions of ~25 km and ~650 °C between 110 and 130 Ma (Fig. 18A). The lack of older preserved ages (i.e., Triassic) from monazite inclusions within garnet indicate that unit Pz_{sch2} is not an exhumed deeper portion of the hanging-wall metamorphic terrane. Plotting peak metamorphic temperatures, muscovite cooling ages, and K-feldspar MDD modeling results together shows rapid cooling of unit Pz_{sch2} immediately after peak metamorphic conditions from ~650 °C to ~350 °C (near the muscovite closure temperature), followed by slow cooling to near isothermal conditions (Fig. 19A). This period of rapid cooling (ca. 110–100 Ma) is interpreted to date the timing of north-northeast–directed motion along the Shala Tala thrust, and emplacement of the high-grade Pz_{sch2} over the low-grade metagraywacke of Pz_{gw2}.

There is an increasing body of evidence for significant middle to Late Cretaceous tectonic activity along the western portion of the Indo-Asian collision zone. To the south, geochronologic investigations along the western Karakoram Mountains (Searle et al., 1990, 1998), southern Karakoram Mountains (Fraser et al., 2001), and eastern Hindu Kush Mountains (Hildebrande et al., 2001) have documented middle to Late Cretaceous metamorphic zircon and monazite ages, as well as numerous Cretaceous (115–80 Ma) plutonic bodies throughout the Karakoram terrane (Debon et al., 1987; Crawford and Searle, 1992; Hildebrande et al., 2001). Middle Cretaceous conglomerates within the Karakoram terrane unconformably overlie deformed Permian to Jurassic deposits (Gaetani et al., 1990, 1993; Gaetani, 1997). To the northeast, thick Cretaceous deposits are found along the margins of the Tarim basin (Hendrix et al., 1992; Sobel, 1999), with apatite fission track data from the northern Tarim basin indicating significant unroofing at 100 ± 20 Ma (Dumitru et al., 2001). These studies, together with our own data, indicate widespread middle Cretaceous crustal thickening and shortening throughout the entire Pamir–western Himalayan syntaxis region and western Tian Shan Mountains. This tectonic activity is interpreted to be related to the Cretaceous closure of the western portion of the Bangong-Nujiang suture between the Lhasa and Qiangtang terranes (Matte et al., 1996), and possible continued underthrusting of the Lhasa terrane beneath the Karakoram (Kapp et al., 2003) (Fig. 18C). It is interesting to note that these contractional events temporally overlap with extensional events in the eastern Altyn Tagh region and eastern China (Ratschbacher et al., 2000; Chen et al., 2003), indicating a complex distribution of coeval extension and contraction in Asia during the Cretaceous.

Cenozoic

Th-Pb ages of ca. 9.3 Ma from monazite inclusions in garnet provide a maximum age

constraint for the timing of peak metamorphic conditions of the Kongur Shan gneisses (Pz_{gn}) of ~8 kbar and 650–700 °C. These results indicate significant Late Miocene crustal thickening along the northeastern margin of the Pamir, interpreted to be related to convergence and thickening along the Main Pamir Thrust. These results also give constraints on the magnitude of extension, indicating ~34 km of east-west extension (assuming a constant fault dip of 40° as observed along the Kongur Shan massif).

MDD thermal modeling of a K-feldspar analysis from the northern footwall of the Kongur Shan normal fault shows a period of rapid cooling initiating at ca. 7–8 Ma, after a period of nearly isothermal conditions since at least the Oligocene (Fig. 17). This rapid cooling event is interpreted to date the initiation of denudation of the footwall along the Kongur Shan normal fault, indicating normal faulting initiated immediately after crustal thickening in the region. Additionally, extrapolation of the MDD modeling results to the present suggest cooling rates for the footwall have been relatively constant since the initiation of extension (Fig. 19B). While a biotite age of 10.1 ± 0.7 Ma ~13 km east of the Kongur Shan fault would suggest that exhumation along the fault initiated slightly earlier along the Kongur Shan massif, the age spectrum is very irregular (Fig. 15E) and is interpreted to be contaminated with excess ^{40}Ar.

Magnitudes of extension along the Qimugang creek portion of the Kongur Shan normal fault are not well constrained. However, assuming a preextensional depth of 10 km (assuming a geotherm of 25 °C/km and a preextensional temperature of 250 °C from the K-feldspar analysis) and a fault dip of 30° for the portion of the fault where the K-feldspar analysis is from indicates ~17 km of east-west extension. This magnitude of east-west extension along the northern portion of the footwall is smaller than that calculated along the Kongur Shan massif. However, the northward decrease in the magnitude of east-west extension may have been accommodated by the Kalagile normal fault. Partitioning of extension between the Kongur Shan and Kalagile normal faults may also explain the smaller magnitude of exhumation for the Qimugang area (~10 km) than for the Kongur Shan massif (~29 km) without requiring significant changes in fault geometry and the magnitude of total extension along fault strike.

The relative chronology of the different fault strands north of the Kongur Shan massif (the Kalagile fault, Qiaklak fault, and Kongur Shan fault) is still unclear. If the Qimugang Creek portion of the fault initiated after east-west extension began in the Kongur Shan massif (Figs. 20A–C), the 7–8 Ma rapid cooling from the K-feldspar analysis is a minimum age for the initiation of east-west extension. Related to this uncertainty is the development of the Qiaklak normal fault (Fig. 5A). If the Kalagile fault represents the original trace of the Kongur Shan fault, it suggests that the Qiaklak fault is the most recent strand of the fault to develop, and the master fault is in the process of propagating westward, excising a portion of the hanging wall (Figs. 20A–C). Alternatively, the Qiaklak fault may be the original trace of the main Kongur Shan normal fault, which has jumped eastward, incising a portion of the footwall (Figs. 20D–F).

Timing of motion along the right-slip Ghez fault (Fig. 5A) is the least-constrained aspect of the Cenozoic evolution of the northern Kongur Shan extensional system. Although the Ghez fault shows no signs of recent activity, three features indicate that motion along the right-slip fault was active during motion along the Kongur Shan normal fault: (1) The Ghez fault truncates units of the Kongur Shan massif; (2) stretching lineations within the mylonitic gneisses of Pz_{gn} adjacent to the Ghez fault are rotated clockwise; and (3) different metamorphic grades are juxtaposed across the Ghez fault. However, whether right-slip motion along the fault initiated before, during, or after initiation of extension is unclear. In any case, development of the Ghez fault may have developed in response to northward translation of the Pamir arc.

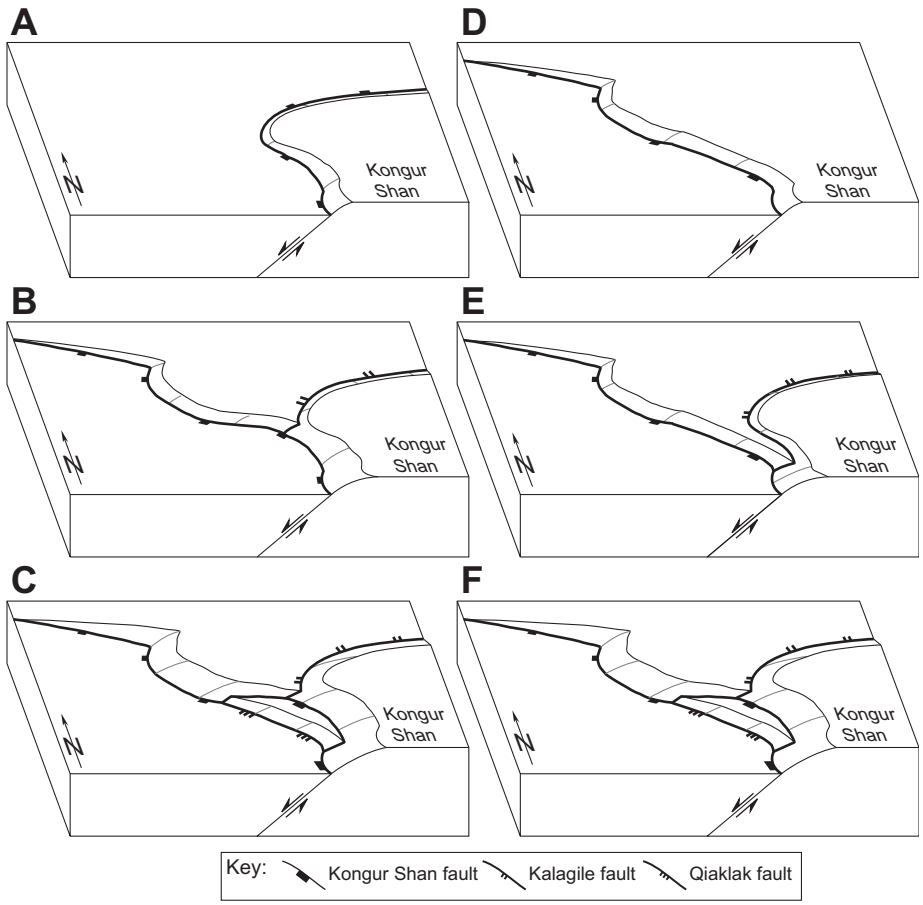

Figure 20. Kinematic models for the development of the northern part of the Kongur Shan extensional system. Model 1: Extension initiates along the Kongur Shan massif but does not extend farther northwest to the Muji fault (A). Extension then propagates northward, along the Qimugang Creek and Muji portions of the fault system (B). Recent excisement of the hanging wall results in development of the Qiaklak fault (C). Model 2: Extension initiates along the Muji, Qimugang creek, and Qiaklak portions of the Kongur Shan extensional system (D). Slip along the Kalagile fault initiates, allowing differential uplift and extension along the footwall (E). Continued evolution of the fault system results in incisement of the footwall, with only minor slip currently being accommodated along the Qiaklak fault (F).

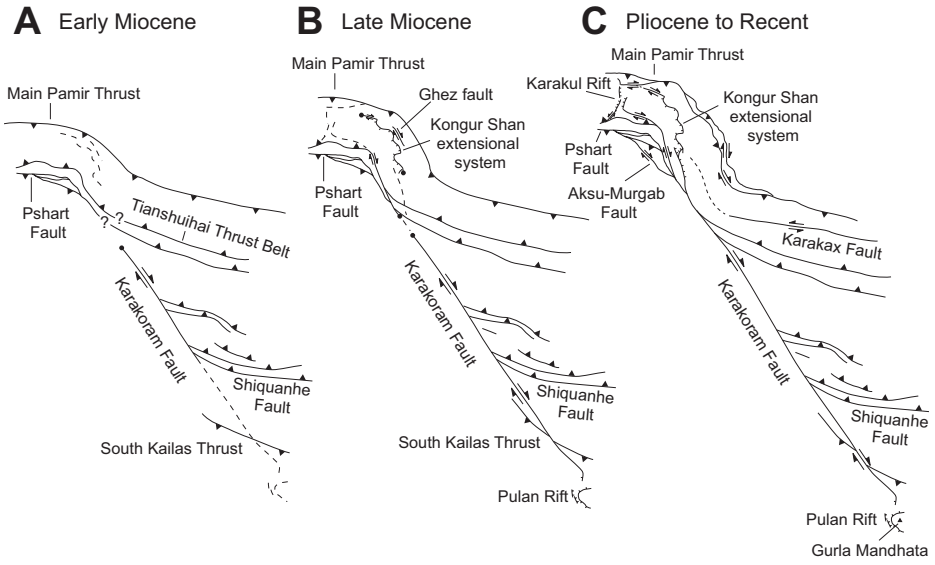

Figure 21. Late Cenozoic evolution of the Kongur Shan extensional system (modified from Murphy et al., 2000, and Cowgill et al., 2003). (A) Early Miocene initiation of Karakoram fault along the western margin of the Tibetan Plateau. The Main Pamir thrust is active, transporting the Pamir salient over the Tarim basin. Shortening along thrust faults occurs within the central Pamir, possibly linked to deformation in the Tianshuihai terrane. (B) Late Miocene Karakoram fault propagates southward, cutting the South Kailas thrust and initiating extension along the Pulan rift system. Immediately after crustal thickening along the northeastern Pamir, east-west extension begins along the northern and central portions of the Kongur Shan extensional system. (C) The Kongur Shan extensional system propagates southward, initiating slip along the Tashkorgan fault, and begins to interact with the northward-propagating Karakoram fault to the south.

East-West Extension in the Pamir

As discussed in the introduction, models for extension in the Pamir fall into three categories of predictions for the spatial and temporal patterns of extension along the Kongur Shan extensional system: (1) extension initiating along the central portion of the fault system, propagating to the north and south (synorogenic extension, e.g., Brunel et al., 1994) (Fig. 3A), (2) extension initiating in the north, propagating southward (radial thrusting of Strecker et al., 1995, or oroclinal bending of Yin et al., 2001) (Figs. 3B and 3C), and (3) extension initiating in the south, propagating northward (propagation of Karakoram fault; Ratschbacher et al., 1994; Murphy et al., 2000) (Fig. 3D).

While we are unable to directly evaluate variations in the magnitude of extension along the central and southern portions of the Kongur Shan extensional system at this time, the large local topographic relief of the footwall (~4 km) along the Kongur Shan normal fault suggest a similar magnitude of extension to that determined along the Kongur Shan massif as far south as the Muztaghata massif. However, slip along the southern Tashkorgan fault appears to diminish significantly southward (Figs. 4E and 4F), and Eocene K-feldspar cooling ages along the northern portion of the Tashkorgan fault footwall (Pan, 1996) indicate minimal late Cenozoic exhumation. These observations indicate that the Tashkorgan fault could not have accommodated the ~34 km of Late Miocene to Recent east-west extension determined for the gneisses of the Kongur Shan massif. Therefore, the predicted pattern of extension for models involving northward propagation of the right-slip Karakoram (maximum extension in the south) is not supported. This observation suggests that east-west extension in the Pamir began independently of (and prior to?) the northward propagation of the Karakoram fault into the region, and that extension in the Pamir is not directly related to the tectonics of southwestern Tibet (cf. Ratschbacher et al., 1994; Murphy et al., 2000). Furthermore, if the right-slip Karakoram fault has propagated into the Pamir relatively recently (i.e., Pliocene), it would suggest that other structures in the Pamir, such as the thrust systems in the Rushan Pshart zone, may also have evolved without being kinematically linked to structures of southwestern Tibet by the Karakoram fault (Fig. 21).

Crustal thickening immediately prior to east-west extension along the Kongur Shan extensional system, and the apparent decrease in magnitude of east-west extension to the north, provide evidence to support the synorogenic extension model of Brunel et al. (1994), in which extension develops as a result of vertical wedge extrusion to accommodate further crustal thickening along the Main Pamir Thrust. However, our observations also leave open the possibility that the total magnitude of east-west extension may be highest along the northern margin of the Pamir. This is due to the uncertainties of the northward termination of the Kalagile normal fault, uncertainties in the subsurface geometries of the different faults, and the possibility that extensional strain is partitioned to the north between the Muji fault and the Karakul rift. Therefore, it is not currently possible to rule out models for east-west extension involving radial spreading along the Main Pamir Thrust (Strecker et al., 1995) or oroclinal bending of the Pamir (Yin et al., 2001). Better constraints on the slip histories of the central and southern segments of the Kongur Shan extensional system, and the Karakul rift to the west, are needed in order to evaluate the applicability of these models.

CONCLUSIONS

Field mapping in conjunction with thermochronology, thermobarometry, and geochronology reveal a complex and protracted tectonic history along the northeastern margin of the Pamir from the Triassic to the present. Hanging-wall schists record development of a Late Triassic to Early Jurassic Buchan metamorphic sequence synchronous with the intrusion of granitic plutons and right-slip ductile shear. This event is interpreted to be related to northward subduction of the Paleo-Tethys ocean beneath the southern margin of Asia, and the development of early Mesozoic arc magmatism and related metamorphism. Pervasive right-slip ductile shear fabrics within the hanging wall support the conclusion by Mattern et al. (1996) that subduction of the Paleo-Tethys ocean was oblique, resulting in dextral shear within the arc system. The significance of Late Jurassic mica cooling ages from the hanging wall, while overlapping with regional tectonic events, is unclear but may be related to motion along the Baoziya thrust.

Amphibolite-facies schists along the northern portion of the footwall record middle Cretaceous crustal thickening at 130–110 Ma. This metamorphic event was followed by rapid exhumation caused by motion along the

northeast-directed Shala Tala thrust, placing the high-grade schists over lower-grade metagraywacke prior to ca. 100 Ma. This event overlaps with numerous events recorded within the Karakoram terrane and the Tarim basin, suggesting the entire western portion of the Indo-Asian collision zone was affected by middle Cretaceous shortening and crustal thickening.

Late Miocene ages from monazite inclusions in garnet from gneisses of the Kongur Shan massif document crustal thickening along the northeastern margin of the Pamir at ca. 9 Ma. Crustal thickening was immediately followed by extension, initiating at 7–8 Ma. Vertical exhumation along the northern Kongur Shan extensional system varies from ~10–11 km along the Qimugang creek portion of the fault to ~29 km along the Kongur Shan massif, with a minimum of ~34 km of east-west extension across the Kongur Shan fault.

Field observations and interpretation of satellite images suggest the magnitude of east-west extension decreases significantly to the south along the Tashkorgan fault segment of the Kongur Shan extensional system. This indicates that recent east-west extension along the Kongur Shan system is not related to northward propagation of the right-slip Karakoram fault as has been previously proposed. Rather, extension is most likely driven by synorogenic extension, radial thrusting along the Main Pamir thrust, or oroclinal bending of the entire Pamir arc.

ACKNOWLEDGMENTS

Discussions with Eric Cowgill, Paul Kapp, and Mike Taylor greatly improved many of the ideas presented in this paper. We thank Marty Grove, Chris Coath, and Kevin McKeegan for assistance with the ion microprobe analyses and Eric Cowgill for assistance with the $^{40}Ar/^{39}Ar$ analyses. This work was supported by National Science Foundation grant EAR-0126122 (to Yin and Manning) and a student grant from the Geological Society of America (to Robinson). Reviews by Mihai Ducea and Matthew Kohn greatly improved the clarity of the presentation and discussion of the metamorphic petrology. The ion microprobe facility at UCLA is partially supported by a grant from the Instrumentation and Facilities Program, Division of Earth Sciences, National Science Foundation.

REFERENCES CITED

Armijo, R., Tapponnier, P., Mercier, J.L., and Han, T.-L., 1986, Quaternary extension in southern Tibet: Field observations and tectonic implications: Journal of Geophysical Research, v. 91, p. 13,803–13,872.

Armijo, R., Tapponnier, P., and Tonglin, H., 1989, Late Cenozoic right-lateral strike-slip faulting in southern Tibet: Journal of Geophysical Research, v. 94, p. 2787–2838.

Arnaud, N.O., Brunel, M., Cantagrel, J.M., and Tapponnier, P., 1993, High cooling and denudation rates at Kongur Shan, eastern Pamir (Xinjiang, China) revealed by $^{40}Ar/^{39}Ar$ alkali feldspar thermochronology: Tectonics, v. 12, p. 1335–1346.

Arrowsmith, J.R., and Strecker, M.R., 1999, Seismotectonic range-front segmentation and mountain-belt growth in the Pamir-Alai region, Kyrgyzstan (India-Eurasia collision zone): Geological Society of America Bulletin, v. 111, p. 1665–1683.

Blisniuk, P.M., and Strecker, M.R., 1996, Kinematics of Holocene normal faulting in the northern Pamir: Eos (Transactions, American Geophysical Union), v. 77, p. F693.

Brunel, M., Arnaud, N., Tapponnier, P., Pan, Y., and Wang, Y., 1994, Kongur Shan normal fault: Type example of mountain building assisted by extension (Karakoram fault, eastern Pamir): Geology, v. 22, p. 707–710.

Burchfiel, B.C., Quidong, D., Molnar, P., Royden, L., Yipeng, W., Peizhen, Z., and Weiqi, Z., 1989, Intracrustal detachment within zones of continental deformation: Geology, v. 17, p. 748–752.

Burg, J.P., and Chen, G.M., 1984, Tectonics and structural zonation of southern Tibet, China: Nature, v. 311, p. 219–223.

Burg, J.-P., and Podladchikov, Y., 2000, From buckling to asymmetric folding of the continental lithosphere: Numerical modeling and application to the Himalayan syntaxses: Geological Society [London] Special Publication 170, p. 219–236.

Burtman, V.S., and Molnar, P., 1993, Geological and geophysical evidence for deep subduction of continental crust beneath the Pamir: Geological Society of America Special Paper 281, p. 76.

Catlos, E.J., Gilley, L.D., and Harrison, T.M., 2002, Interpretation of monazite ages obtained via in situ analysis: Chemical Geology, v. 188, p. 193–215.

Cebula, G.T., Kunk, M.J., Mehnert, H.H., Naeser, C.W., Obradovich, J.D., and Sutter, J.F., 1986, The Fish Canyon Tuff, a potential standard for the ^{40}Ar-^{39}Ar and fission-track dating methods: Terra Cognita, v. 6, p. 139–140.

Chen, X., Yin, A., Gehrels, G.E., Cowgill, E.S., Grove, M., Harrison, T.M., and Wang, X.-F., 2003, Two phases of Mesozoic north-south extension in the eastern Altyn Tagh range, northern Tibetan Plateau: Tectonics, v. 22, p. 1053, doi: 10.1029/2001TC001336.

Cherniak, D.J., Watson, E.B., Grove, M., and Harrison, T.M., 2004, Pb diffusion in monazite: A combined RBS/SIMS study: Geochimica et Cosmochimica Acta, v. 68, p. 829–840.

Cowgill, E., Yin, A., Harrison, T.M., Grove, M., and Wang, X.-F., 2001, Oligocene intiation of the Central Altyn Tagh Fault System inferred from $^{40}Ar/^{39}Ar$ K-feldspar thermochronology: Eos (Transactions, American Geophysical Union), v. 82, p. F1125.

Cowgill, E., Yin, A., Harrison, T.M., and Xiao-Feng, W., 2003, Reconstruction of the Altyn Tagh fault based on U-Pb geochronology: Role of back thrusts, mantle sutures, and heterogeneous crustal strength in forming the Tibetan Plateau: Journal of Geophysical Research, v. 108, 2346, doi: 10.1029/2002JB002080.

Crawford, M.B., and Searle, M.P., 1992, Field relations and geochemistry of pre-collisional (India-Asia) granitiod magmatism in the central Karakoram, northern Pakistan: Tectonophysics, v. 206, p. 171–192.

Debon, F., Le Fort, P., Dautel, D., Sonet, J., and Zimmerman, J.L., 1987, Granites of western Karakorum and northern Kohistan (Pakistan): A composite Mid-Cretaceous to Upper Cenozoic magmatism: Lithos, v. 20, p. 19–40.

Dewey, J.F., Shackleton, R.M., Chengfa, C., and Yiyin, S., 1988, The tectonic evolution of the Tibetan Plateau: Royal Society of London Philosophical Transactions, v. 327, p. 379–413.

Dewey, J.F., Cande, S., and Pitman, W.C., III, 1989, Tectonic evolution of the India/Eurasia collision zone: Eclogae Geologicae Helvetiae, v. 82, no. 3, p. 717–734.

Dumitru, T.A., Zhou, D., Chang, E.Z., Graham, S.A., Hendrix, M.S., Sobel, E.R., and Carroll, A.R., 2001, Uplift, exhumation, and deformation in the Chinese Tian Shan, *in* Hendrix, M.S., and Davis, G.A., eds., Paleozoic and Mesozoic tectonic evolution of central Asia: From continental assembly to intracontinental deformation: Boulder, Colorado, Geological Society of America Memoir 194, p. 71–99.

Dunlap, W.J., Weinberg, R.F., and Searle, M.P., 1998, Karakoram fault zone rocks cool in two phases: Geological Society [London] Journal, v. 155, p. 903–912.

England, P., and Houseman, G.A., 1985, Role of lithospheric strength heterogeneities in the tectonics of Tibet and neighbouring regions: Nature, v. 315, p. 297–301.

Fan, G., Ni, J.F., and Wallace, T.C., 1994, Active tectonics of the Pamirs and Karakoram: Journal of Geophysical Research, v. 99, p. 7131–7160.

Fraser, J.E., Searle, M.P., Parrish, R.R., and Nobel, S.R., 2001, Chronology of deformation, metamorphism, and magmatism in the southern Karakoram Mountains: Geological Society of America Bulletin, v. 113, p. 1443–1455.

Gaetani, M., 1997, The Karakorum Block in Central Asia, from Ordovician to Cretaceous: Sedimentary Geology, v. 109, p. 339–359.

Gaetani, M., Garzanti, E., Jadoul, F., Nicora, A., Tintori, A., Pasini, M., and Khan, K.S.A., 1990, The North Karakorum side of the Central Asia geopuzzle: Geological Society of America Bulletin, v. 102, p. 54–62.

Gaetani, M., Jadoul, F., Erba, E., and Garzanti, E., 1993, Jurassic and Cretaceous orogenic events in the North Karakoram: Age constraints from sedimentary rocks, *in* Treloar, P.J., and Searle, M.P., eds., Himalayan tectonics: Geological Society [London] Special Publication 74, p. 39–52.

Grove, M., and Bebout, G.E., 1995, Cretaceous tectonic evolution of coastal southern California: Insights from the Catalina Schist: Tectonics, v. 14, p. 1290–1308.

Harrison, T.M., Heizler, M.T., Lovera, O.M., Chen, W., and Grove, M., 1994, A chlorine disinfectant for excess argon released from K-feldspar during step heating: Earth and Planetary Science Letters, v. 123, p. 95–104.

Harrison, T.M., Ryerson, F.J., LeFort, P., Yin, A., Lovera, O.M., and Catlos, E.J., 1997, A Late Miocene-Plicocen origin for the Central Himalayan inverted metamorphism: Earth and Planetary Science Letters, v. 146, p. E1–E7.

Harrison, T.M., Grove, M., McKeegan, K.D., Coath, C.D., Lovera, O.M., and Le Fort, P., 1999, Origin and episodic emplacement of the Manaslu intrusive complex, Central Himalaya: Journal of Petrology, v. 40, p. 3–19.

Harrison, T.M., Catlos, E.J., and Montel, J.-M., 2002, U-Th-Pb dating of phosphate minerals, *in* Kohn, M.J., et al., eds., Phosphates: Geochemical, geobiological, and materials importance: Reveiws in mineralogy and geochemistry: Washington, D.C., Mineralogical Society of America, p. 523–558.

Hendrix, M.S., Graham, S.A., Carroll, A.R., Sobel, E.R., McKnight, C.L., Schulein, B.J., and Wang, Z., 1992, Sedimentary record and climatic implications of recurrent deformation in the Tian Shan: Evidence from Mesozoic strata of the north Tarim, south Junggar, and Turpan basins, northwest China: Geological Society of America Bulletin, v. 104, p. 53–79.

Hildebrande, P.R., Nobel, S.R., Searle, M.P., Waters, D.J., and Parrish, R.R., 2001, Old origin for an active mountain range: Geology and geochronology of the eastern Hindu Kush, Pakistan: Geological Society of America Bulletin, v. 113, p. 625–639.

Hodges, K.V., 2000, Tectonics of the Himalaya and southern Tibet from two perspectives: Geological Society of America Bulletin, v. 112, p. 324–350.

Houseman, G., and England, P., 1996, A lithospheric-thickening model for the Indo-Asian collision, *in* Yin, A., and Harrison, T.M., eds., The tectonic evolution of Asia: New York, Cambridge University Press, p. 3–17.

Johnson, M.W.R., 2002, Shortening budgets and the role of continental subduction during the India-Asia collision: Earth and Planetary Science Letters, v. 59, p. 2002.

Kapp, P., Murphy, M.A., Yin, A., Harrison, T.M., Lin, D., and Jinghui, G., 2003, Mesozoic and Cenozoic tectonic evolution of the Shiquanhe area of western Tibet: Tectonics, v. 22, 1029, doi: 10.1029/2001TC001332.

Khan, M.A., Jan, M.Q., and Weaver, B.L., 1993, Evolution of the lower arc crust in Kohistan, N., Pakistan: Temporal arc magmatism through early, mature and intra-arc rift settings, *in* Treloar, P.J., and Searle, M.P., eds., Himalayan tectonics: Geological Society [London] Special Publication 74, p. 123–138.

Le Pichon, X., Fournier, M., and Jolivet, L., 1992, Kinematics, topography, shortening, and extrusion in the India-Eurasia collision: Tectonics, v. 11, p. 1085–1098.

Lovera, O.M., Grove, M., Harrison, T.M., and Mahon, K.I., 1997, Systematic analysis of K-feldspar $^{40}Ar/^{39}Ar$ step heating results I: Significance of activation energy determinations: Geochimica et Cosmochimica Acta, v. 61, p. 3171–3192.

Lovera, O.M., Grove, M., and Harrison, T.M., 2002, Systematic analysis of K-feldspar $^{40}Ar/^{39}Ar$ step heating results II: Relevance of laboratory argon diffusion properties to nature: Geochimica Et Cosmochimica Acta, v. 66, p. 1237–1255.

Madin, I.P., Lawrence, R.D., and Ur-Rehman, A., 1989, The northwestern Nanga Parbat-Haramosh Massif: Evidence for crustal uplift at the northwestern corner of the Indian Craton: Boulder, Colorado, Geological Society of America Special Paper 232, p. 169–182.

Maheo, G., Guillot, S., Blichert-Toft, J., Rolland, Y., and Pecher, A., 2002, A slab breakoff model for the Neogene thermal evolution of South Karakorum and South Tibet: Earth and Planetary Science Letters, v. 195, p. 45–58.

Matte, P., Tapponnier, P., Arnaud, N., Bourjot, L., Avouac, J.P., Vidal, P., Liu, Q., Pan, Y., and Wang, Y., 1996, Tectonics of Western Tibet, between the Tarim and the Indus: Earth and Planetary Science Letters, v. 142, p. 311–330.

Mattern, F., and Schneider, W., 2000, Suturing of the Proto- and Paleo-Tethys oceans in the western Kunlun (Xinjiang, China): Journal of Asian Earth Sciences, v. 18, p. 637–650.

Mattern, F., Schneider, W., Li, Y., and Li, X., 1996, A traverse through the western Kunlun (Xinjiang, China): Tentative geodynmamic imlications for the Paleozoic and Mesozoic: Geologishe Rundschan, v. 85, p. 7705–7722.

Molnar, P., and Tapponnier, P., 1975, Cenozoic tectonics of Asia: Effects of a continental collision: Science, v. 183, p. 419–426.

Montel, J.M., Kornprobst, J., and Veilzeuf, D., 2000, Preservation of old U-Th-Pb ages in shielded monazite: Example from the Beni Bousera Hercynian kinzigites (Morocco): Journal of Metamorphic Geology, v. 18, p. 335–342.

Murphy, M.A., Yin, A., Harrison, T.M., Durr, S.B., Chen, Z., Ryerson, F.J., Kidd, W.S.F., Wang, X., and Zhou, X., 1997, Did the Indo-Asian collision alone create the Tibetan plateau?: Geology, v. 25, p. 719–722.

Murphy, M.A., Yin, A., Kapp, P., Harrison, T.M., Ling, D., and Jinghui, G., 2000, Southward propagation of the Karakoram fault system, southwest Tibet: Timing and magnitude of slip: Geology, v. 28, p. 451–454.

Murphy, M.A., Yin, A., Kapp, P., Harrison, T.M., Manning, C.E., Ryerson, F.J., Lin, D., and Jinghui, G., 2002, Structural evolution of the Gurla Mandhata detachment system, sourthwest Tibet: Implications for the eastward extent of the Karakoram fault system: Geological Society of America Bulletin, v. 114, p. 428–447.

Neil, E.A., and Houseman, G.A., 1997, Geodynamics of the Tarim Basin and the Tian Shan in central Asia: Tectonics, v. 16, p. 571–584.

Paces, J.B., and Miller, J.D., 1993, Precise U-Pb age of the Duluth Complex and related mafic intrusions, northeastern Minnesota: Geochronological insights in physical, petrogenetic, paleomagnetic, and tectonomagmatic processes associated with the 1.1 Ga midcontinent rift system: Journal of Geophysical Research, v. 98, p. 13,997–14,013.

Pan, Y., 1992, Introduction to integrated scientific investigation on Karakoram and Kunlun Mountains: Beijing, China Meteorological Press, 92 p.

Pan, Y., 1996, Geological evolution of the Karakoram and Kunlun Mountains: Beijing, Seismological Press, 288 p.

Pavlis, G.L., and Das, S., 2000, The Pamir-Hindu Kush seismic zone as a strain marker for flow in the upper mantle: Tectonics, v. 19, p. 103–115.

Pavlis, T.L., Hamburger, M.W., and Pavlis, G.L., 1997, Erosional processes as a control on the structural evolution of an actively deforming fold and thrust belt: An example from the Pamir-Tien Shan region, central Asia: Tectonics, v. 16, p. 810–822.

Pegler, G., and Das, S., 1998, An enhanced image of the Pamir-Hindu Kush seismic zone from relocated earthquake hypocenters: Geophysical Journal International, v. 134, p. 573–595.

Peltzer, G., and Tapponnier, P., 1988, Formation and evolution of strike-slip faults, rifts, and basins during the India-Asia collision: An experimental approach: Journal of Geophysical Research, v. 93, p. 15,085–15,117.

Powell, R., Holland, T., and Worley, B., 1998, Calculating phase diagrams involving solid solutions via non-linear equations, with examples using THERMOCALC: Journal of Metamorphic Geology, v. 116, p. 557–588.

Ratschbacher, L., Frisch, W., Liu, G., and Chen, C.C., 1994, Distributed deformation in southern and western Tibet during and after the India-Asian collision: Journal of Geophysical Research, v. 99, p. 19,917–19,945.

Ratschbacher, L., Hacker, B.R., Webb, L.E., McWilliams, M.O., Ireland, T., Dong, S., Calvert, A., Chateigner, D., and Wenk, H.R., 2000, Exhumation of the unltrahigh-pressure continental crust in east central China: Cretaceous and Cenozoic unroofing and the Tan-Lu fault: Journal of Geophysical Research, v. 105, p. 13,303–13,338.

Renne, P.R., Deino, A.L., Walter, R.C., Turrin, B.D., Swisher, C.C., Becker, T.A., Curtis, G.H., Sharp, W.D., and Jaouni, A.R., 1994, Intercalibration of astronomical and radioisotopic time: Geology, v. 22, p. 783–786.

Renne, P.R., Swisher, C.C., Deino, A.L., Karner, D.B., Owens, T.L., and DePaolo, D.J., 1998, Intercalibration of standards, absolute ages and uncertainties in $^{40}Ar/^{39}Ar$ dating: Chemical Geology, v. 145, p. 117–152.

Robinson, D.M., Dupont-Nivet, G., Gehrels, G.E., and Zhang, Y., 2003, The Tula uplift, northwestern China: Evidence for regional tectonism of the northern Tibetan Plateau during Mesozoic-early Cenozoic time: Geological Society of America Bulletin, v. 115, p. 35–47.

Rumelhart, P.E., Yin, A., Cowgill, E., Butler, R., Zhang, Q., and Wang, X.-F., 1999, Cenozoic vertical-axis rotation of the Altyn Tagh fault system: Geology, v. 27, p. 819–822.

Schneider, D.A., Edwards, M.A., Kidd, W.S.F., Asif Khan, M., Seeber, L., and Zeitler, P.K., 1999, Tectonics of Nanga Parbat, western Himalaya; synkinematic plutonism within the doubly vergent shear zones of a crustal-scale pop-up structure: Geology, v. 27, p. 999–1002.

Searle, M.P., 1996, Geological evidence against large-scale pre-Holocene offsets along the Karakoram Fault: Implications for the limited extrusion of the Tibetan plateau: Tectonics, v. 15, p. 171–186.

Searle, M.P., Parrish, R.R., Tirrul, R., and Rex, D.C., 1990, Age of crystallization and cooling of the K2 gneiss in the Baltoro Karakoram: Geological Society [London] Journal, v. 147, p. 603–606.

Searle, M.P., Weinberg, R.F., and Dunlap, W.J., 1998, Transpressional tectonics along the Karakoram fault zone, northern Ladakh: Constraints on Tibetan extrusion, *in* Holdsworth, R.E., et al., eds., Continental transpressional and transtensional tectonics: Geological Society [London] Special Publication 74, p. 307–326.

Searle, M.P., Khan, M.A., Fraser, J.E., Gough, S.J., and Jan, M.Q., 1999, The tectonic evolution of the Kohistan-Karakoram collision belt along the Karakoram Highway transect, north Pakistan: Tectonics, v. 18, p. 929–949.

Seeber, L., and Pecher, A., 1998, Strain partitioning along the Himalayan arc and the Nanga Parbat antiform: Geology, v. 26, p. 791–794.

Şengör, A.M.C., and Natal'in, B.A., 1996, Paleotectonics of Asia: Fragments of a synthesis, *in* Yin, A., and Harrison, T.M., eds., The tectonic evolution of Asia: New York, Cambridge University Press, p. 486–640.

Smith, H.A., and Giletti, B.J., 1997, Lead diffusion in monazite: Geochimica et Cosmochimica Acta, v. 61, p. 1047–1055.

Sobel, E.R., 1999, Basin analysis of the Jurassic-Lower Cretaceous southwest Tarim basin, northwest China: Geological Society of America Bulletin, v. 111, p. 709–724.

Sobel, E.R., and Dumitru, T.A., 1997, Thrusting and exhumation around the margins of the western Tarim basin during the India-Asia collision: Journal of Geophysical Research, v. 102, p. 5043–5063.

Sobel, E.R., Arnaud, N., Jolivet, M., Ritts, B.D., and Brunel, M., 2001, Jurassic to Cenozoic exhumation history of the Altyn Tagh range, northwest China, constrained by $^{40}Ar/^{39}Ar$ and apatite fission track thermochrnology, *in* Hendrix, M.S., and Davis, G.A., eds., Paleozoic and Mesozoic tectonic evolution of central Asia: From continental assembly to intracontinental deformation: Boulder, Colorado, Geological Society of America Memoir 194, p. 247–267.

Spear, F.S., and Cheney, J.T., 1989, A petrogenetic grid for pelitic schists in the system SiO_2-Al_2O_3-FeO-MgO-K_2O-H_2O: Contributions to Mineralogy and Petrology, v. 101, p. 149–164.

Stacey, J.S., and Kramers, J.D., 1975, Approximation of terrestrial lead isotope evolution by a two-stage model: Earth and Planetary Science Letters, v. 26, p. 207–221.

Strecker, M.R., Frisch, W., Hamburger, M.W., Ratschbacher, L., Semiletkin, S., Zamoruyev, A., and Sturchio, N., 1995, Quaternary deformation in the Eastern Pamirs, Tadzhikistan and Kyrgyzstan: Tectonics, v. 14, p. 1061–1079.

Tapponnier, P., Mattauer, M., Proust, F., and Cassaigneau, C., 1981, Mesozoic ophiolites, sutures, and large-sale tectonic movements in Afghanistan: Earth and Planetary Science Letters, v. 52, p. 355–371.

Tapponnier, P., Peltzer, G., Le Dain, A.Y., Armijo, R., and Cobbold, P., 1982, Propagating extrusion tectonics in Asia: New insights from simple experiments with plasticine: Geology, v. 10, p. 611–616.

Treloar, P.J., and Izatt, C.N., 1993, Tectonics of the Himalayan collision between the Indian Plate and the Afghan Block: A synthesis, *in* Treloar, P.J., and Searle, M.P., eds., Himalayan tectonics: Geological Society [London] Special Publication 74, p. 69–87.

Wing, B.A., Ferry, J.M., and Harrison, T.M., 2003, Prograde destruction and formation of monazite and allanite during contact and regional metamorphism of pelites: Petrology and geochronology: Contributions to Mineralogy and Petrology, v. 145, no. 2, p. 228–250.

Xiao, W., Windley, B.F., Hao, J., and Li, J., 2002a, Arc-ophiolite obduction in the Western Kunlun Range (China): Implications for the Paleozoic evolution of central Asia: Geological Society [London] Journal, v. 159, p. 517–528.

Xiao, W.J., Windley, B.F., Chen, H.L., Zhang, G.C., and Li, J.L., 2002b, Carboniferous-Triassic subduction and accretion in the western Kunlun, China: Implications for the collisional and accretionary tectonics of the northern Tibetan Plateau: Geology, v. 30, p. 295–298.

Yin, A., 2000, Mode of Cenozoic east-west extension in Tibet suggesting a common origin of rifts in Asia during the Indo-Asian collision: Journal of Geophysical Research, v. 105, p. 21,745–21,759.

Yin, A., and Harrison, T.M., 2000, Geologic evolution of the Himalayan-Tibetan orogen: Annual Review of Earth and Planetary Sciences, v. 28, p. 211–280.

Yin, A., Robinson, A., and Manning, C.E., 2001, Oroclinal bending and slab-break-off causing coeval east-west extension and east-west contraction in the Pamir-Nanga Parbat syntaxsis in the past 10 m.y.: Eos (Transactions, American Geophysical Union), v. 82, p. F1124.

Yin, A., Rumelhart, P.E., Butler, R., Cowgill, E., Harrison, T.M., Foster, D.A., Ingersoll, R.V., Qing, Z., Xian-Qiang, Z., Xiao-Feng, W., Hanson, A., and Raza, A., 2002, Tectonic history of the Altyn Tagh fault system in northern Tibet inferred from Cenozoic sedimentation: Geological Society of America Bulletin, v. 114, p. 1257–1295.

Yin, J., and Bian, Q., 1992, Geologic map of the Karakoram-Western Kunlun and adjacent regions: Beijing, Science Press, scale 1:2,000,000.

Youngun, Y., and Hsu, K.J., 1994, Origin of the Kunlun Mountains by arc-arc and arc-continent collisions: The Island Arc, v. 3, p. 75–89.

Zeitler, P.K., Koons, P.O., Bishop, M.P., Chamberlain, C.P., Craw, D., Edwards, M.A., Hamidullah, S., Janm, M.Q., Khan, M.A., Khattak, M.U.K., Kidd, W.S.F., Mackie, R.L., Meltzer, A.S., Park, S.K., Pecher, A., Poage, M.A., Sarker, G., Schneider, D.A., Seeber, L., and Shroder, J.F., 2001, Crustal reworking at Nanga Parbat, Pakistan: Metamorphic consequences of thermal-mechanical coupling facilitated erosion: Tectonics, v. 20, p. 712–728.

Manuscript Received by the Society 4 April 2003
Revised Manuscript Received 31 October 2003
Manuscript Accepted 25 November 2003

Printed in the USA